CCFE-PR(15)49

I. Lupelli, A. Malizia, M. Richetta, L.A. Poggi, J.F. Ciparisse, M.Gelfusa
and P. Gaudio

Simulations and Experiments to reach Numerical Multiphase Informations for Security Analysis on Large Volume Vacuum Systems like Tokamaks

Simulations and Experiments to reach Numerical Multiphase Informations for Security Analysis on Large Volume Vacuum Systems like Tokamaks

I. Lupelli[1], A. Malizia[2], M. Richetta[2], L.A. Poggi[2], J.F. Ciparisse[2], M.Gelfusa[2] and P. Gaudio[2]

[1]EURATOM/CCFE Association, Culham Science Centre, Abingdon, United Kingdom
[2]Associazione EURATOM-ENEA, Department of Industrial Engineering, University of Rome "Tor Vergata", Via del Politecnico 1, 00133 Rome, Italy

SIMULATIONS AND EXPERIMENTS TO REACH NUMERICAL MULTIPHASE INFORMATIONS FOR SECURITY ANALYSIS ON LARGE VOLUME VACUUM SYSTEMS LIKE TOKAMAKS

I. Lupelli[1], A. Malizia[2], M. Richetta[2], L.A. Poggi[2], J.F. Ciparisse[2], M.Gelfusa[2] and P. Gaudio[2]

[1] EURATOM/CCFE Association, Culham Science Centre, Abingdon, United Kingdom

[2] Associazione EURATOM-ENEA, Department of Industrial Engineering, University of Rome "Tor Vergata", Via del Politecnico 1, 00133 Rome, Italy

Abstract

Dust re-suspension as a consequences of LOVA (Loss Of Vacuum Accident) or LOCA (Loss Of Coolant Accident) situations inside a nuclear fusion plant (ITER-like) is an important issue for the workers' safety and for the security of the plant. The dust size expected inside tokamaks like ITER is of the order of microns (0.1-1000 μm). Analysis of the thermo fluid-dynamics and transport phenomena involved during an accidental pressurization transitory is necessary in order to set up and operated tokamaks with careful consideration of the potential risks. Computational Fluid Dynamics (CFD) study of LOVA scenario is a challenging task for today numerical methods and models because it involves 3D large vacuum volumes, multiphase flows ranging from highly supersonic to nearly incompressible and heat transfer simultaneously. Present work deals with development and experimental validation of CFD model, which simulates the complex thermo fluid-dynamic field and gives some indication about internal hazardous dust mobilization phenomena during vessel filling at near vacuum conditions, for supporting first instant of LOVA safety analysis. The research activity had been carried out in the framework of EURATOM-ENEA Association - University of Rome Tor Vergata Quantum Electronics Plasma Physics and Materials (QEPM) Research Group.

Keywords: CFD, fusion, LOVA, multiphase, nuclear, security

Introduction

Large volume vacuum systems are used worldwide and its accidents have a relevant economical

and safety impact [1]. A loss of vacuum accident (LOVA) can result in a fast pressurization of the vacuum vessel (VV) and consequent mobilization and dispersion of hazardous internal material through the braches. Analysis of the thermo fluid-dynamics and transport phenomena involved during an accidental pressurization transitory is necessary in order to set up and operate tokamaks [2-5]. Numerical codes are generally widely used to model and evaluate various safety issues from normal operation up to largest credible accident situations [6]. Validated CFD codes are recognized as an important tool in order to evaluate the acceptable level of risk for workers, population and ambient [7, 23]. The CFD study of LOVA scenario is a challenging task [8-10] for today numerical codes and models because it involves 3D vacuum volumes, multiphase flows ranging from highly supersonic to nearly incompressible and heat transfer simultaneously [11]. Development of specific codes and additional validation of existing ones are required. A code for safety analysis in large vacuum systems should take into account:

- Pressurization of a volume at low initial pressure;
- Critical flows ranging from highly supersonic to nearly incompressible;
- Turbulent multiphase flows;
- Heat transfer between walls, continuum phase and dust.

Accuracy is also required in order to provide essential data to design safety features.. The development and validation of the CFD model presented in this work and related experimental activities are carried out in strong correlation in order both to understand the capabilities of computational code and to predict correctly flow characteristics during LOVAs. STARDUST facility [12-21, 24] was chosen both for model development and for validation. Furthermore, a preliminary dust mobilization model in case of a LOVA is developed. Research activity had been carried out in the framework of EURATOM – ENEA Association - University of Rome Tor Vergata QEPM Research Group. Simulations were performed at ENEA-GRID facility. Experimental protocol, description of STARDUST facility, development and validation of CFD model of LOVA, and a preliminary numerical analysis for dust mobilization, are presented.

2. Experimental Protocol

Numerical results are compared to experimental data provided by STARDUST facility (Fig.1) that is selected both for the model development phase and validation case. The aim of STARDUST development was designed to experimentally study thermal and flow fields and dust mobilization mechanisms expected in a LOVA. In particular STARDUST reproduces a LOVA event, at different pressurization rates (**Error! Reference source not found.**), due to a

small air leakage for two different positions of the leak, at two different high in the vessel, high (Valve A) and low level (Valve B) (Fig.1).

	Pressurization rate [Pa/s]	Inlet Flow rate [l/min]
MC (25°C)	100	8
	300	22
	500	41
AC (110°C)	100	10
	300	26,5
	500	5

Table 1 Pressurization and flow rates for LOVAs experiment

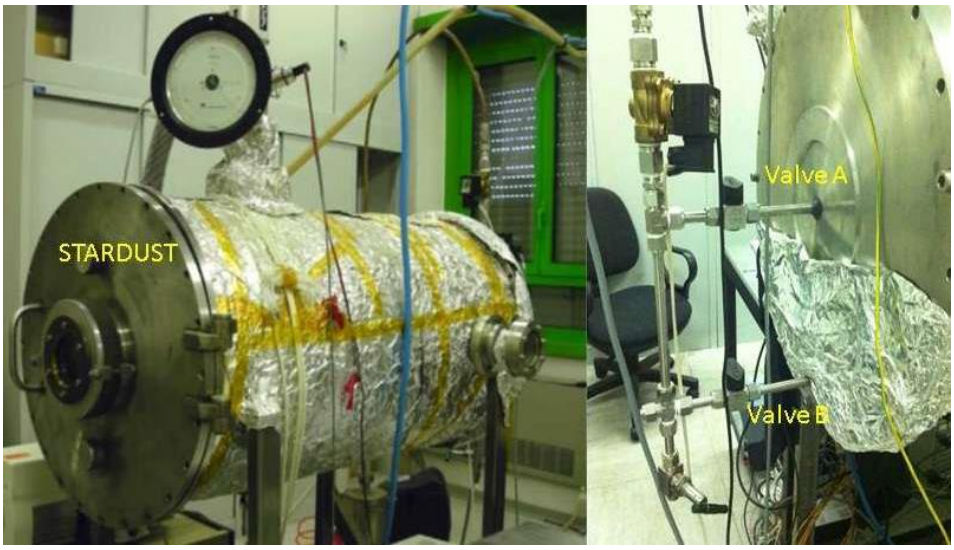

Fig.1 STARDUST Facility (on the left) and Valves A and B (on the right) used to reproduce, LOVAs at different height

This facility also allows evaluation of obstacles influence and wall temperature on dust re-suspension during maintenance (MC) and accident conditions (AC). Performed experiments are LOVA simulations [43] and Vessel Filling Experiments (VFEs). VFEs allow pressurization rate and mean temperature profile determination inside STARDUST starting from two different internal initial pressure (100 Pa, 1000 Pa) and wall temperature (MC 25°C, AC 110°C [12,13]).

These experiments are useful for turbulence models and optimal grids resolution selection, chosen comparing experimental results with analytic unsteady solution of the pressurization process (Transient Generalized Unsteady Model, TGUM). Functional scheme and experimental protocol for VFEs are shown in Fig. 2 and Fig.3.

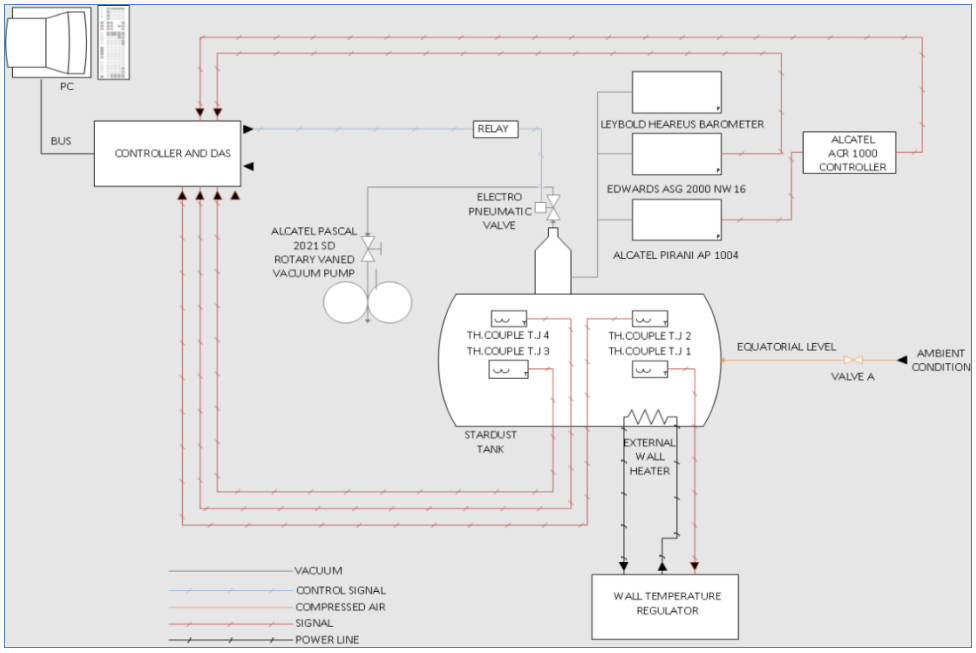

Fig.2 STARDUST functional scheme for VFEs

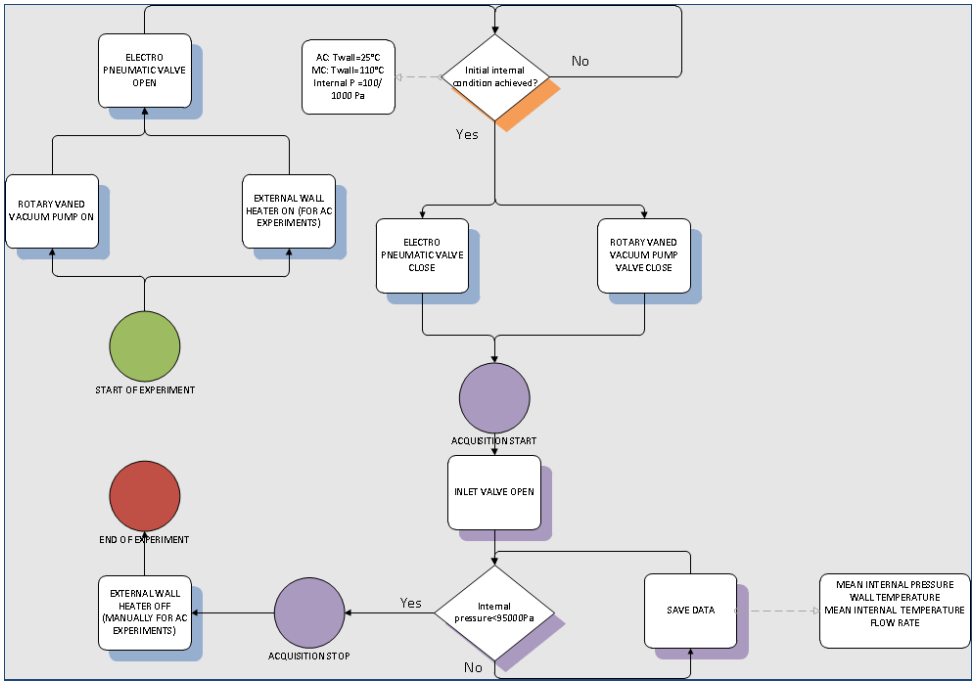

Fig.3 VFEs experimental protocol

VFEs, propaedeutic for LOVAs and finalized to CFD model development, are focused on the pressurization and mean temperature profile inside STARDUST starting from two different internal initial pressure (100 and 1000 Pa), both for AC e MC, with an atmospheric pressure at the inlet boundary (**Error! Reference source not found.**). Only for preliminary dust mobilization model, Valve B is used in this work.

	Initial vessel pressure
MC (25°C)	100 Pa
	1000 Pa
AC (110°C)	100 Pa
	1000 Pa

Table 2 Initial internal pressure for VFEs experiment

2.1. Experimental facility main features for numerical simulations

STARDUST facility [12-21] cylindrical stainless-steel vessel main dimensions, instrumentation and diagnostics (including pressure control, flow-rate control, air velocity determination using pressure transducers, and heating system) are presented in [43].

Before starting the test, the vacuum level (~ 100 or 1000 Pa) was obtained inside the vessel by pumping. At this vacuum level the Knudsen number is <1 (Table 3), also in the worst test case condition (100Pa, 293K). This is very important because traditional continuum CFD techniques are often invalid for analyzing gas flows with Knudsen ~1.

Mean free path and Knudsen number		
Vessel Pressure	100	Pa
Vessel Temperature	293	K
Boltzmann Constant	1,38E-23	J/K
Loschmidt Constant	2,47E+22	molecules/m^3
Mean Molecule Diameter (Air)	3,40E-10	m
Mean Free Path	79	μm

Knudsen	8,75E-03	

Table 3 Mean free path and Knudsen number for STARDUST

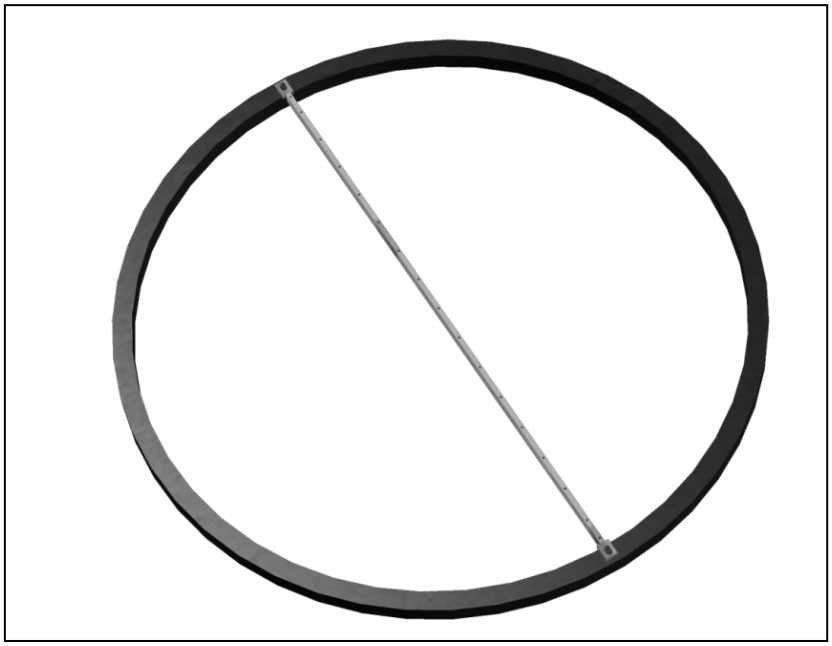

Fig.4 Probe support system

Pressure transducers allows to determinate local differential pressure, hence it is possible to calculate air punctual velocity as a function of that pressure, local temperature, and static pressure of the chamber. Transducers are positioned inside the vessel according to Table 4:

Probe Coordinates				
Name	**Plane**	**x[m]**	**y[m]**	**z[m]**
A	Equatorial	0.01	0.248	0
B		0.2275	0.248	0
C		0.455	0.248	0
D		0.6825	0.248	0
E		0.6825	0.248	-0.243
F		0.455	0.248	-0.243
G		0.2275	0.248	-0.243

H	Symmetry	0.01	0.486	0
I		0.2275	0.486	0
L		0.455	0.486	0
M		0.6825	0.486	0
N		0.6825	0.0095	0
O		0.455	0.0095	0
P		0.2275	0.0095	0
Q		0.01	0.0095	0
Directions				
Name	**Plane**	**Point**		
Line 1	Equatorial	B-G		
Line 2		C-F		
Line 3		D-E		
Line 4	Symmetry	H-Q		
Line 5		I-P		
Line 6		L-O		
Line 7		M-N		

Table 4 Pressure transducers positions

The axisymmetric sketch of the STARDUST geometry with the pressure transducers positions is reported in Fig.5.

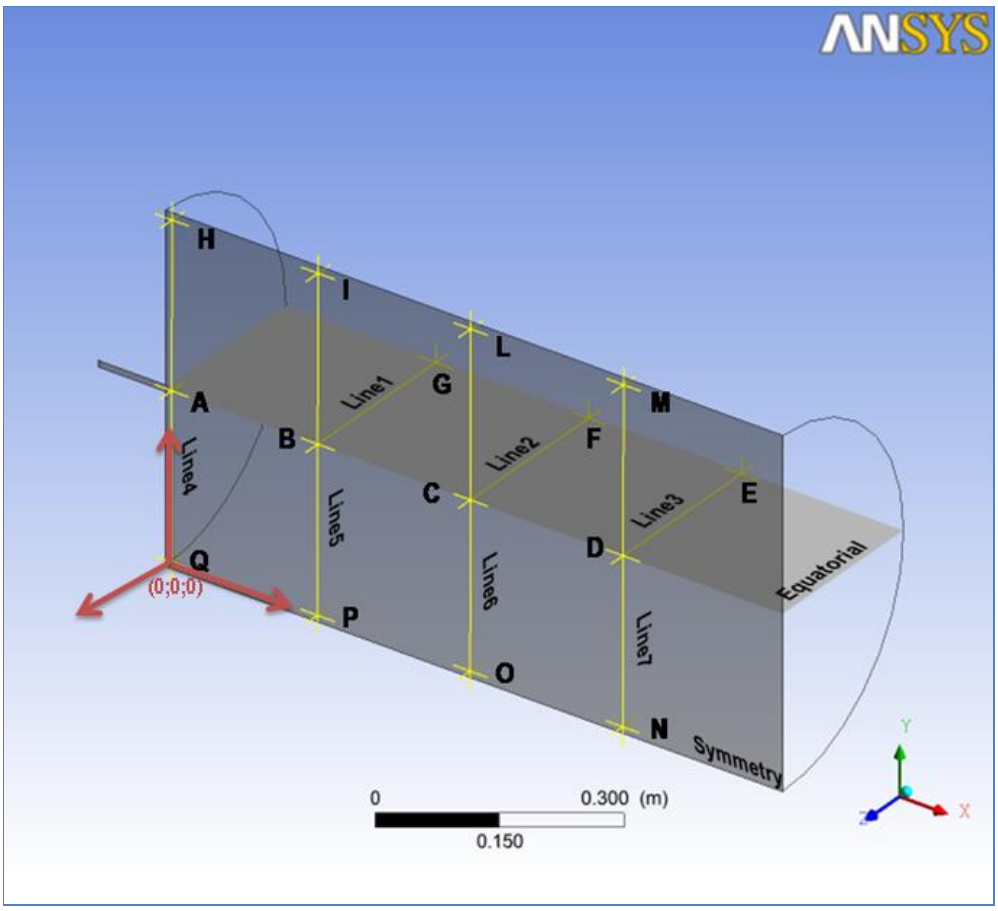

Fig.5 Pressure transducers position inside STARDUST

3. Development of a CFD model for loss of vacuum accident analysis

3.1. Numerical setting

TGUM adiabatic (Adiab) and isothermal (Iso) pressurization model of a confined volume has been adopted [25]. Analysis involves time-dependent fluid flow and energy transfer. Unsteady forms of mass and energy conservation equations are required to be solved in addition to the flow-rate equation and equation of state. The numerical scheme solves mass and energy conservation equations in conjunction with the equation of state by an implicit successive substitution procedure. A control volume (Fig.6) based procedure [26] is developed to solve the transient mass and energy conservation equations in conjunction with isentropic flow-rate equation and equation of state.

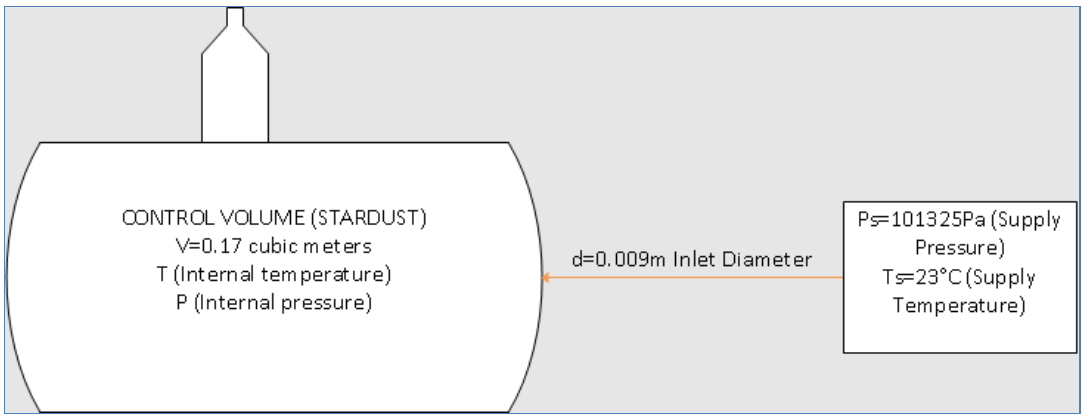

Fig.6 Control volume for vessel filling process

Mass conservation equation (1) at the current time step (t+Δt) can be written as:

$$m_{t+\Delta t} = m_t + \dot{m}_{t+\Delta t}\Delta t \tag{1}$$

The term on the left side represents the mass of air in the vessel at the current time step (t+Δt). The first term on the right side represents the mass of air at the previous time step (t). The second term on the right side represents the amount of mass entering into the vessel during the interval considered. Mass flow rate at the current time step can be expressed by the relationship (2) between stagnation pressure of the supply line (P_s) and static pressure in the vessel (P):

$$\dot{m} = \sqrt{\frac{2\gamma}{(\gamma-1)} P_S \rho_S \left(\frac{p}{P_S}\right)^{\frac{2}{\gamma}} \left(1 - \frac{p}{P_S}\right)^{\frac{\gamma-1}{\gamma}}} \tag{2}$$

It may be noted here that an implicit method requires flow-rate at the current time step. Energy conservation equation at (t+Δt) (3) can be written as:

$$(m \cdot u)_{t+\Delta t} = (m \cdot u)_t + \dot{m}_{t+\Delta t} h_s \Delta t \tag{3}$$

The first term on the right side of equation represents the energy at the previous time step. The amount of energy entering the control volume, during the current time step, is represented by the second term in the equation. Temperature at the current time step is calculated (4) from the internal energy:

$$T_{t+\Delta t} = \frac{u_{t+\Delta t}}{c_v} \tag{4}$$

For isothermal model equation above is not required to be solved. Temperature is constant and equals the supply temperature during the entire pressurization process. We must take in account some simplifying assumptions:

- During transient pressurization thermodynamic equilibrium exists inside the vessel and with respect to the surroundings;
- The gas (air) is ideal with constant specific heat. The equation of state for an ideal (5) gas is used to calculate chamber's pressure;

$$P_{t+\Delta t} = \frac{m_{t+\Delta t} R T_{t+\Delta t}}{V} \tag{5}$$

- Air in the vessel is at rest;
- Spatially uniform thermodynamic properties;
- 1D and isentropic flow through inlets;
- Constant cross sectional diameter (d) of the inlet.

Since mass conservation equation has a non-linear term, and it is coupled with the equation of state, a numerical solution is needed. An implicit successive substitution method is used to solve governing equations. Fig.7 shows the information flow diagram.

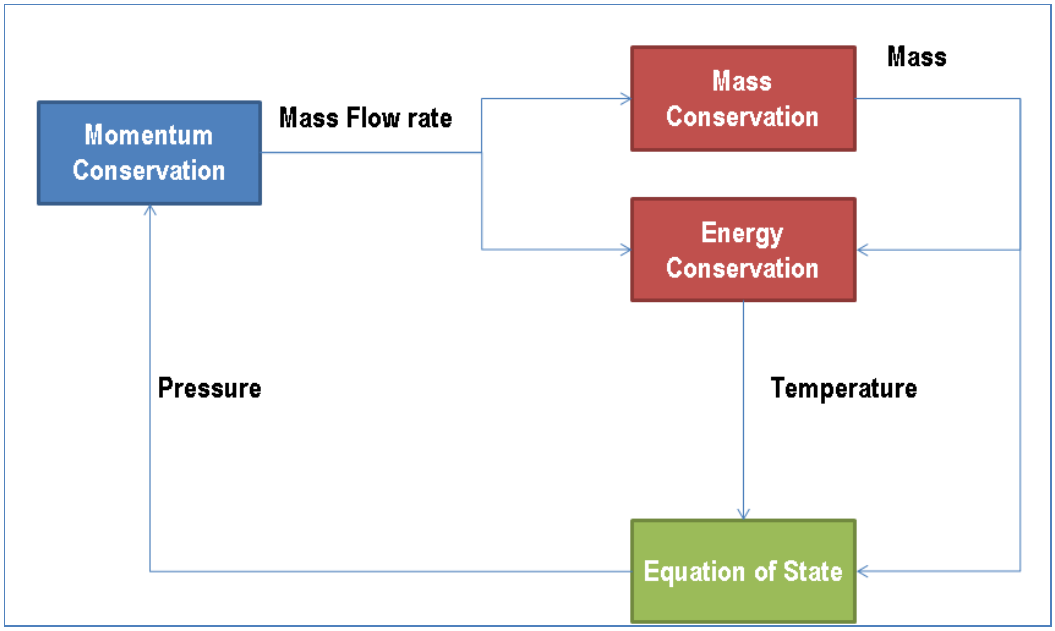

Fig.7 Flow diagram of the successive substitution algorithm

Solution steps are summarized:

1. at initial time (t=0) internal pressure, temperature and mass are set according to the experimental data provided by STARDUST experiment (**Error! Reference source not found.**);
2. sequent time-step (t=t+Δt) begins updating variables in the current time-step;
3. iteration loop for the current time-step begins guessing values of the variables. Usually in unsteady computation, the values prevailing at the previous time-step are the best guess;
4. resident mass $m_{t+\Delta t}$ calculation from the mass conservation equation;
5. internal energy calculation from the energy conservation equation;
6. internal pressure of the chamber calculation from the equation of state;
7. calculation of fractional difference in pressure between successive iterations;
8. if the fractional difference is larger than a pre-specified small number known as the convergence criterion (convergence criterion for the present problem is set to 10^{-6}), the iteration loop is repeated (steps 3 to 7) until the solution is converged.

Results of predicted pressure history for the TGUM during adiabatic (Adiab) and isothermal (Iso) pressurization are shown in Fig.8 for 100/1000 Pa and for maintenance (MC) and accident (AC) condition.

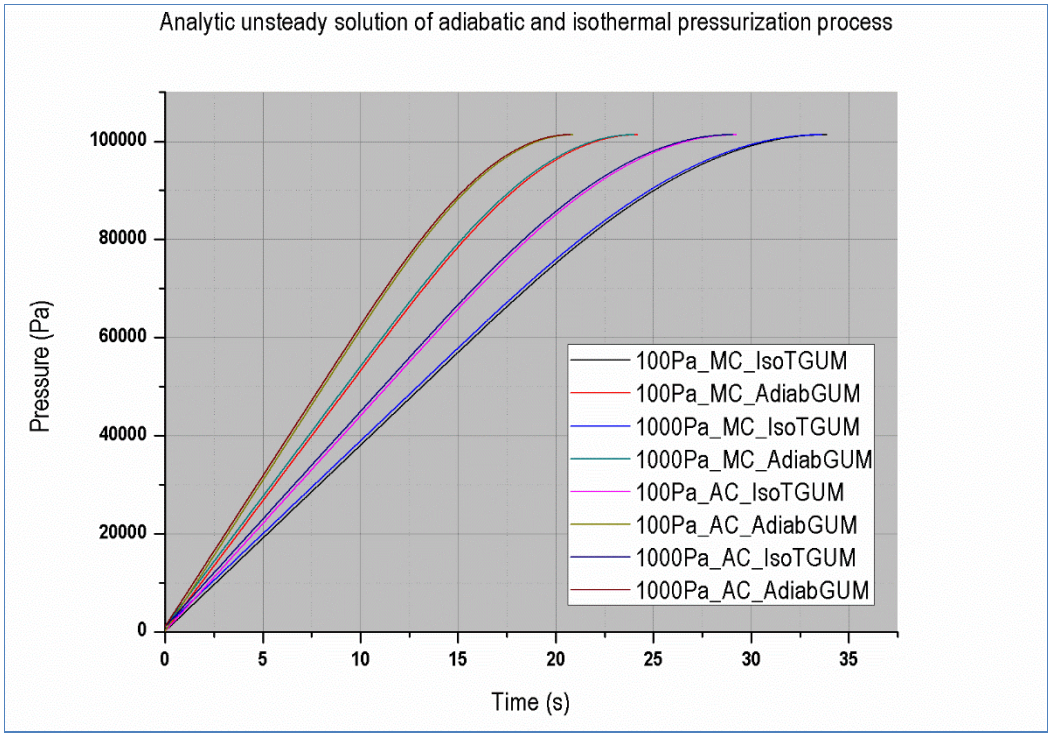

Fig.8 Analytic unsteady solution of adiabatic and isothermal pressurization process

The adiabatic case, as expected, presents the highest slope, while the slope is lower for the

isothermal condition. The variation of initial internal pressure seems not to influence significantly the pressurization process. The internal temperature seems to increase the slope of the pressurization curve.

The numerical simulation proposed [27,28] for the CFD model development phase is related to the transient simulation of the pressure and mean temperature profile inside a 3D geometry similar to the STARDUST starting from different conditions (see **Error! Reference source not found.**) with atmospheric static pressure at the inlet boundary of the equatorial port level (Valve A, Fig.1). Regarding the turbulence modeling, different approaches are compared during the simulations: The Reynolds-averaged Navier–Stokes equations (RANS), considering both the k-ε and RNG k-ε, and Large eddy simulation (LES) approach. The grid [29] independency of the CFD model is proven by running the computation on at least three different grids. Safety analyses related to pressurization of vessels are modeled with a rather coarse discretization including about 10^3 mesh points. However, some safety issues were clearly identified where a much finer resolution of the simulation tools was required. These issues are often related to situations where the 3D aspects of the flow and the geometrical effects have a significant influence. Turbulence and dust mobilization is a common feature of these flows. CFD tools are then required to model small scale mixing phenomena with a fine space resolution including 10^5 to 10^7 mesh points. A 3D axial-symmetric domain was considered in performing the CFD simulations, as shown in Fig.9 where the cartesian coordinate reference system is also reported. The spatial discretization consists of hexahedral elements both for the vessel domain and the horizontal inlet pipe. The 3D axial-symmetric domain was discretized using three structured grids (Fig.2). The number of cells used to mesh the STARDUST vessel and the inlet region are summarized in **Error! Reference source not found.**. The first grid (Coarse) was a mesh of 22.644 cells and radially refined only near the inlet axis of the domain to accurately solve the flow and the temperature distribution in these regions. The second grid (Fine) was a structured mesh of 249.084 cells. For LES, the computational grid must be chosen so that the separation of the resolved and the subgrid-scales occurs in the inertial subrange of the energy spectrum. Accordingly, the Fine grid size has been chosen to be one order of magnitude larger than that of the smallest scales (Kolmogorov scales) according to Mukunda et al. [30]. The third grid (Extra Fine) was a mesh of 2.264.402 cells radially refined both near the axis and near the lateral wall.

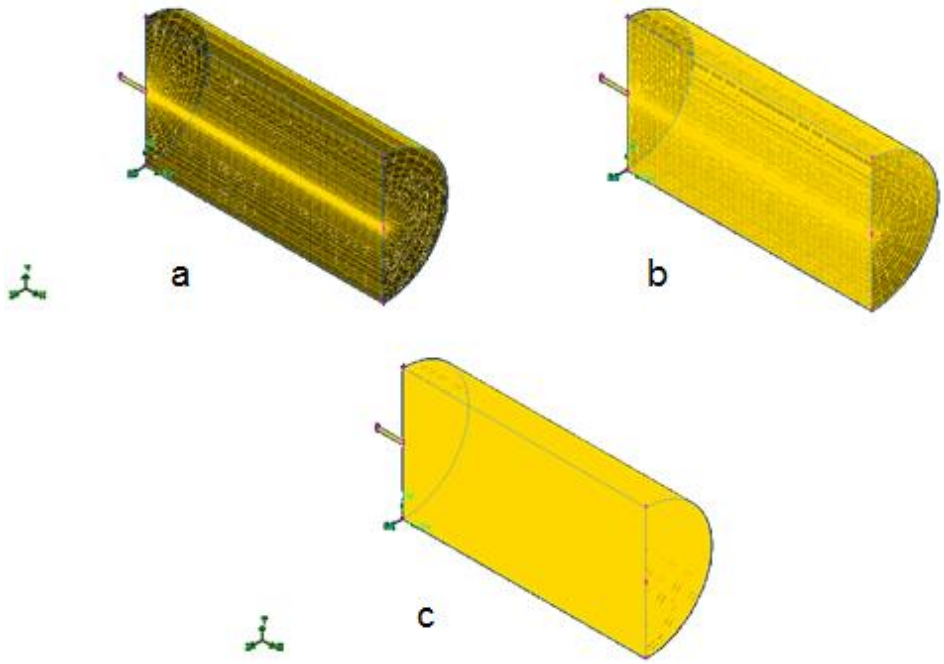

Fig.2 Structured grid a) Coarse, b) Fine, c) Extra Fine

Grid dimension	
Name	Number of cells
Coarse	22.644
Fine	249.084
Ext. Fine	2.264.402

Table 5 Grid dimension

The y^+ constraint required by the different turbulence model is achieved by using a solution automatic adaptive refinement, as cells can be added where they are needed in the mesh (Fig.**3**).

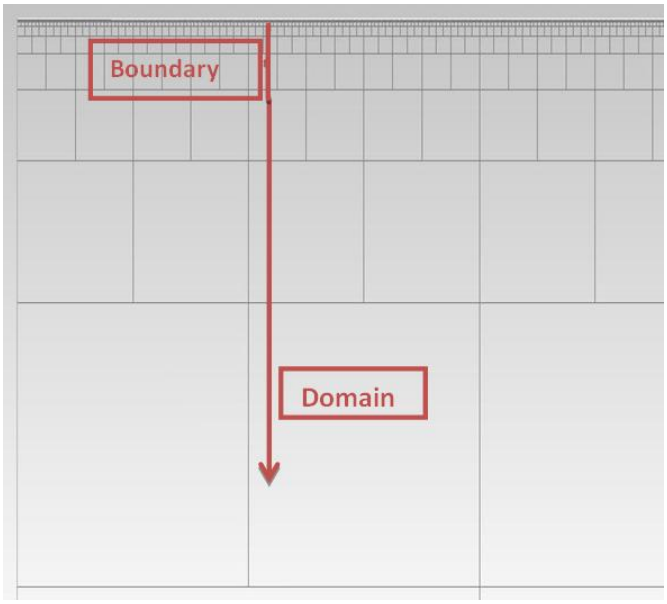

Fig.3 Grid refinement at boundary layer (Inlet pipe)

Fig.**4** shows the fluid domain and the different boundary conditions imposed.

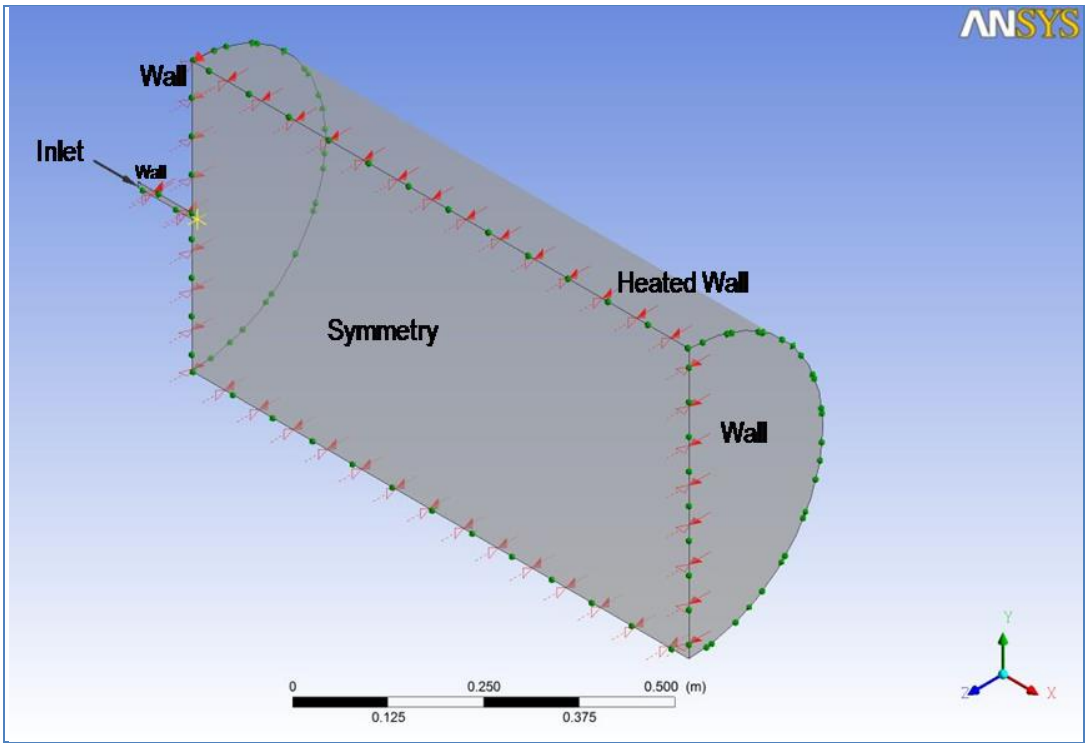

Fig.4 Boundary condition

A symmetry plane passes through the jet axis. The symmetry plane boundary condition imposes constraints that "mirror" the flow on either side of it. The normal velocity component at the symmetry plane boundary is set to zero ($\mathbf{u_n} = 0$) and the scalar variable gradients normal to the boundary are also set to zero ($d\phi/d\mathbf{n} = 0$). At the inlet surface pressure and temperature are imposed. The total pressure, equal to 101326 Pa is specified as an inlet boundary condition and the solver computes the static pressure needed to properly close the boundary condition. The temperature is set to room temperature equal to 296 K. No-slip boundary conditions were assumed for all the walls. The velocity of the fluid at the wall boundary is set to zero for all simulation, so the boundary condition for the velocity becomes $u_{wall} = 0$. The effect of heat transfer between walls and ambient is taken into account except for the heated wall in MC and AC experiment where a temperature condition is set. A convection heat transfer coefficient was considered for all the walls of the vessel according to empirical relation (6) where the Nusselt number $\overline{Nu}$ is considered as a function of Prandtl (Pr) and Reynolds (Re) numbers [31]:

$$\overline{Nu} = \left[0.825 + \frac{0.387Re^{1/6}}{\left[1+(0.492/Pr)^{9/16}\right]^{8/27}}\right] \quad (6)$$

Heat flux at the wall boundary is calculated according to $q_w = h_c(T_b - T_{nw})$ where h_c is a specified heat transfer coefficient (from $\overline{Nu}$), T_b is the specified boundary temperature, (that is, outside the fluid domain) and T_{nw} is the temperature at the internal near-wall boundary element center node. The condition of the environment is equal to T=296 K and P=101325 Pa (ambient condition). The heated wall temperatures are maintained for both cases constant at fixed temperature both for MC (Twall=25°C) and AC (Twall=110°C) during the whole transient. As internal initial conditions, two different initial conditions, 100 and 1000 Pa, were considered in order to verify the effect of pressure on the pressurization of the vessel during the transient. The operating fluid used in the simulations was dry air assumed initially at rest. The density of the fluid is evaluated using the standard Redlich Kwong real gas and the other thermodynamic properties are considered variable. The selection of an appropriate time-step size is essential in order to obtain good convergence. A too large time-step will lead to poor convergence and a too small time-step will lead to larger computational time. Within a given time-step the transport equations are solved during an iteratively process until the convergence criteria is met for all equations. In these simulations, a constant time-step of 1 $x10^5$ s is used. Each time-step is considered to be converged when the maximum residual value was no higher than 1 $x10^{-6}$. In the present work, for the model development, six simulations with effects of three different grids and

three different turbulence models were investigated. The performed simulations can be summarized in the test matrix presented in Table 6.

Test Matrix	
Grid	**Turbulence model**
Coarse	k-ε
	RNG k-ε
	LES
Fine	k-ε
	RNG k-ε
	LES
Ext. Fine	LES

Table 6: Test matrix of the performed simulations

3.2 Validation of a CFD model for Loss Of Vacuum Accidents

The LOVAs is performed with the turbulence model, grid size and near wall treatment selected from the results of previous model development (see results section). The fluid domain and the different boundary conditions imposed are the same of model development phase but now the external air enters into the vessel with a fixed flow rate according to the desired constant pressurization rate (see **Error! Reference source not found.**). On the basis of the available experimental data, the inlet flow rate inlet function can be simplified, with a conservative approximation, in a linear increase of the pressurization rate for the first second of the transient and a constant pressurization rate for the remaining transient (

Fig**.5**). This simplification takes into account the time necessary for the opening of the inlet valve and the time necessary to reach the regime of the mass flow rate.

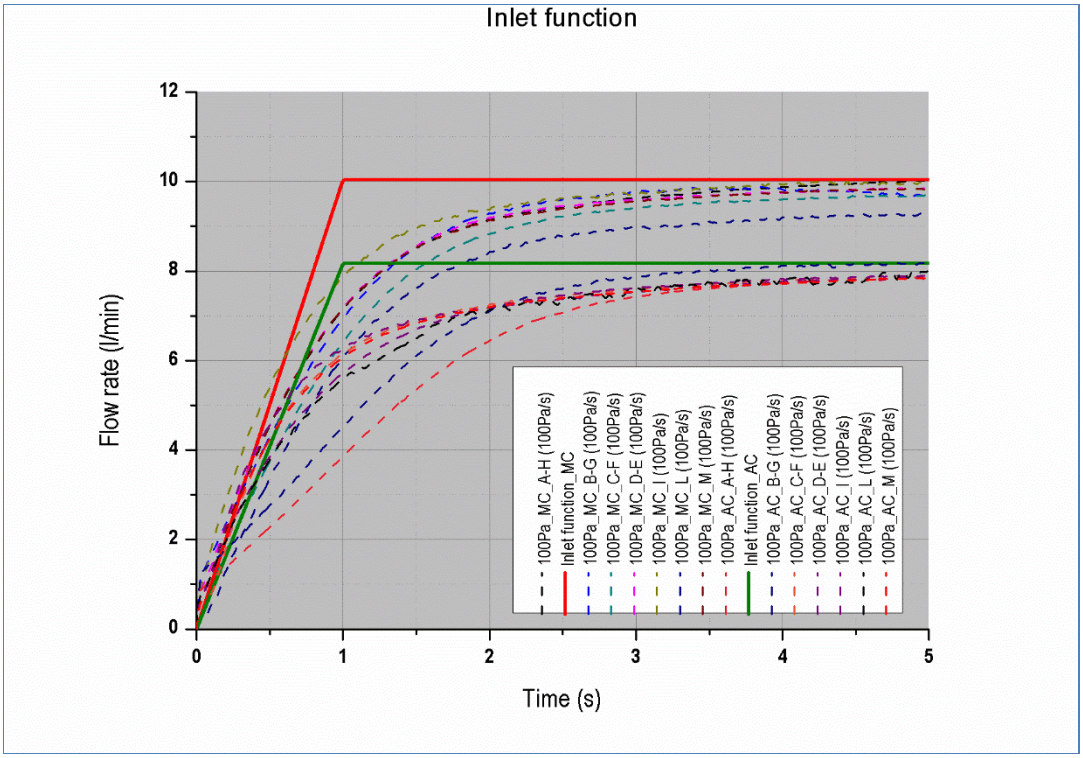

Fig.5 Air flow rate time trend imposed as inlet boundary condition (Inlet function)

The inlet air temperature is set to the environmental value (T=296K). No-slip boundary conditions were assumed at all the walls. The effect of heat transfer between walls and ambient is taken into account except for the heated wall in MC and AC experiment where a temperature condition is set. The ambient condition is T=296 K and P=101325 Pa. The heated wall are maintained at constant temperature both for MC (Twall=25°C) and AC (Twall=110°C) during the whole transient. Two different initial internal conditions (100 Pa and 1000 Pa) were considered in order to verify the effect of pressure on the velocity during the transient. The values of initial internal condition are provided by STARDUST data (Table 7). The operating fluid used in the simulations is dry air assumed initially at rest. The density of the fluid is evaluated using the standard Redlich Kwong real gas and the other thermodynamic properties were considered variable according to internal database.

Thermophysical properties and representative system parameters					
Molar mass (Air)	M			28.966	kg/kmol
Relative Gas Constant	R			287	J/KgK
Supply conditions					
Temperature	T_0	23	°C	296	K

Pressure	p_0	2.80	bar	280000	Pa
Density (Ideal Gas Model)	ρ0			3.30	kg/m^3
Specific heat capacity at constant pressure (100-1000K)	Cp0			966	J/KgK
Specific heat capacity at constant volume (100-1000K)	Cv0			679	J/KgK
Cp/Cv ratio	γ0			1.42	
Dynamic viscosity (Sutherland)	η0			1.82E-05	Pa*s
Kinematic viscosity	ν0			5.51E-06	m^2/s
Speed of sound	vs0			348	m/s
Critical pressure	pc0			146853	Pa
Vessel condition					
Temperature	T1	22.9	°C	296	K
Pressure	p_1	1	mbar	100	Pa
Density (Ideal Gas Model)	ρ1			0.001657	kg/m^3
Specific heat capacity at constant pressure (100-1000K)	Cp1			966	J/KgK
Specific heat capacity at constant volume (100-1000K)	Cv1			679	J/KgK
Cp/Cv ratio	γ1			1.42	
Dynamic viscosity (Sutherland)	η1			1.82E-05	Pa*s
Kinematic viscosity	ν1			1.10E-02	m^2/s
Speed of sound	vs1			348	m/s
Critical pressure	pc1			74	Pa
Internal wall temperature		25	°C	298	K

Table 7: Typical dataset provided by STARDUST

In A. Malizia et al. [43] it is showed that the influence of the turbulence model on pressurization rate is negligible [26-39]. The curves obtained in the performed simulations demonstrate that the LES computations are consistent and in general showed better agreement with the experiments than RANS [44]. Furthermore, the code predicts the oscillating phenomenon that is not observed

in the experimental curve probably because of the low response speed of pressure probes. The presence of pressure oscillations is due to the inertia phenomena involved in this kind problem and could cause the release of dust from the vessel. For each case pressurization rates (from 2 to 4 s) are shown in Tables 8-11 together with the time to reach the ambient pressure (i.e. filling time). The effect of grid size can be appreciated too (Table 8 and Table 9 for 100 Pa and 1000 Pa of initial internal pressure respectively and for 25°C, Table 10 and Table 11 for 100 Pa and 1000 Pa of initial internal pressure respectively and for 110°C).

Effect of different turbulence models and grid dependence (Pvessel=100 Pa, Twall=25°C)				
Reference Value	**Pressurization rate 2-4 s [Pa/s]**	**Δ Pressurization Rate**	**Filling time [s]**	**Δ Filling Time**
Experimental (STARDUST)	4405	-	22,5	-
Isothermal Unsteady Model	3551	-19%	26,97	20%
Adiabatic Unsteady Model	4972	13%	19,26	-14%
Turbulence Model	**Pressurization rate 2-4 s [Pa/s]**	**Δ Pressurization Rate**	**Filling time [s]**	**Δ Filling Time**
K- ε (Fine grid)	4962	13%	21	-7%
RNG K- ε (Fine grid)	4962	13%	21	-7%
LES (Fine grid)	4427	1%	22,1	-2%
Grids	**Pressurization rate 2-4 s [Pa/s]**	**Δ Pressurization Rate**	**Filling time [s]**	**Δ Filling Time**
Coarse (LES)	2927	-34%	21	-7%
Fine (LES)	4427	1%	22,1	-1,8%
Extra Fine (LES)	4427	1%	22,1	-1,8%

Table 8: Effect of different turbulence models and grid dependence (Pvessel=100 Pa, Twall=25°C)

Effect of different turbulence models and grids (Pvessel=1000 Pa, Twall=25°C)				
Reference Value	**Pressurization rate 2-4 s [Pa/s]**	**Δ Pressurization Rate**	**Filling time [s]**	**Δ Filling Time**

Experimental (STARDUST)	4612	-	22,0	-
Isothermal Unsteady Model	3551	-23%	26,7	21%
Adiabatic Unsteady Model	4972	8%	19,1	-13%
Turbulence Model	**Pressurization rate 2-4 s [Pa/s]**	**Δ Pressurization Rate**	**Filling time [s]**	**Δ Filling Time**
K- ε (Fine grid)	5181	12%	20,0	-9%
RNG K- ε (Fine grid)	5181	12%	20,0	-9%
LES (Fine grid)	4637	1%	22,5	2%
Grids	**Pressurization rate 2-4 s [Pa/s]**	**Δ Pressurization Rate**	**Filling time [s]**	**Δ Filling Time**
Coarse (LES)	6490	41%	20,0	-9%
Fine (LES)	4637	1%	22,5	2%
Extra Fine (LES)	4637	1%	22,5	2%

Table 9: Effect of different turbulence models and grids (P vessel=1000 Pa, Twall=25°C)

Effect of different turbulence models and grid dependence (Pvessel=100 Pa, Twall=110°C)				
Reference Value	**Pressurization rate 2-4 s [Pa/s]**	**Δ Pressurization Rate**	**Filling time [s]**	**Δ Filling Time**
Experimental (STARDUST)	5115	-	18,50	-
Isothermal Unsteady Model	4390	-14%	23	27%
Adiabatic Unsteady Model	6146	20%	17	-9%
Turbulence Model	**Pressurization rate 2-4 s**	**Δ Pressurization**	**Filling time**	**Δ Filling**

	[Pa/s]	Rate	[s]	Time
K- ε (Fine grid)	6737	32%	17,3	-6%
RNG K- ε (Fine grid)	6737	32%	17,3	-6%
LES (Fine grid)	5157	1%	17,9	-3%
Grids	**Pressurization rate 2-4 s [Pa/s]**	**Δ Pressurization Rate**	**Filling time [s]**	**Δ Filling Time**
Coarse (LES)	3251	-36%	18,4	-1%
Fine (LES)	5157	1%	17,9	-3%
Extra Fine (LES)	5157	1%	17,9	-3%

Table 10: Effect of different turbulence models and grid dependence (Pvessel=100 Pa, Twall=110°C)

Effect of different turbulence models and grids (Pvessel=1000 Pa, Twall=110°C)				
Reference Value	**Pressurization rate 2-4 s [Pa/s]**	**Δ Pressurization Rate**	**Filling time [s]**	**Δ Filling Time**
Experimental (STARDUST)	5355	-	18,5	-
Isothermal Unsteady Model	4390	-18%	23,2	26%
Adiabatic Unsteady Model	6146	15%	16,6	-10%
Turbulence Model	**Pressurization rate 2-4 s [Pa/s]**	**Δ Pressurization Rate**	**Filling time [s]**	**Δ Filling Time**
K- ε (Fine grid)	7034	31%	16,5	-11%
RNG K- ε (Fine grid)	7034	31%	16,5	-11%
LES (Fine grid)	5402	1%	18,2	-2%
Grids	**Pressurization rate 2-4 s [Pa/s]**	**Δ Pressurization Rate**	**Filling time [s]**	**Δ Filling Time**
Coarse (LES)	7209	35%	17,5	-5%
Fine (LES)	5402	1%	18,2	-2%
Extra Fine (LES)	5402	1%	18,2	-2%

Table 11: Effect of different turbulence models and grids (Pvessel=1000 Pa, Twall=110°C)

The numerical results with heat transfer at walls show that the pressurization process has an adiabatic unsteady behavior while the isothermal unsteady model overestimation is clearly visible. From these results it can be deducted that for pressurization transient the effects related to heat transfer through the walls to the environment can be neglected. The filling time is also under-estimated for adiabatic unsteady case. Obtained results for the pressurization rate and filling time show good agreement with experimental data. The difference between the finest grid and the coarse grid show an unstable LES solution for the coarse grid that seems prone to instability in low flow regions. We can claim that no great improvements seem to be made by use the extra fine grid. The fine grid 249.084 cells are selected as a suitable compromise between accuracy and computational efficiency (1.6 day of CPU time for 1 s of physical time). From the streamlines analysis, after vacuum breakdown, the jet [39] generates a vortex structures that roll up several times and the inlet gas particles follow larger one which brushes and interacts with all boundaries. In Fig.13 velocity streamlines are shown.

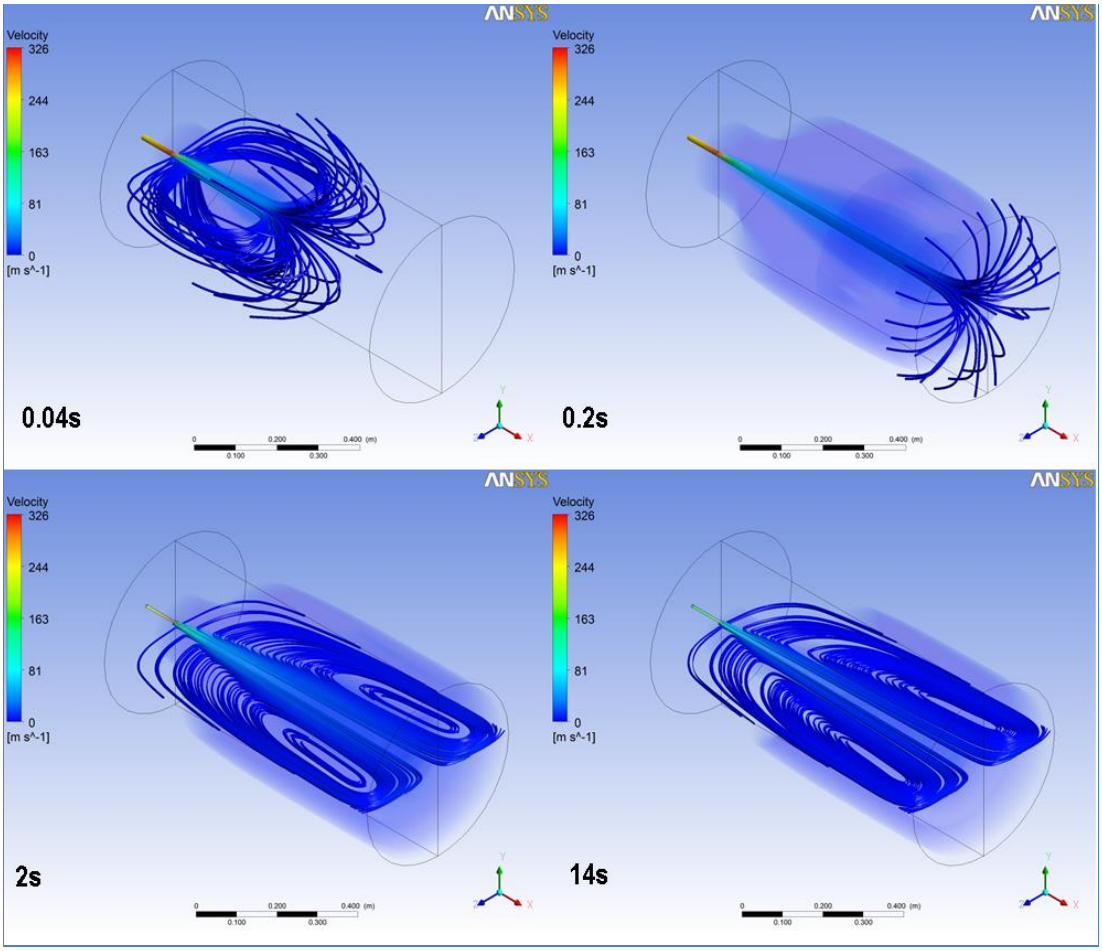

Fig.6 Velocity streamlines

Fig.14 shows that the turbulent kinetic energy is dissipated totally in the first part of the vessel. Temperature transient for the 3D model is evaluated for the whole STARDUST vessel (average volumetric static temperature) and is showed in Fig.15.

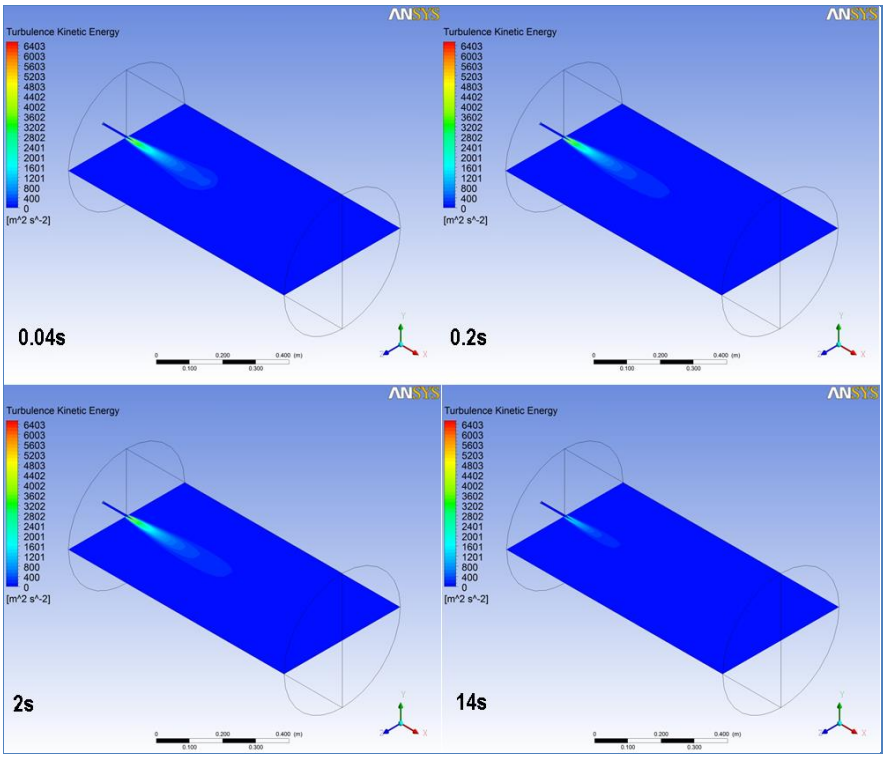

Fig.7 Turbulence kinetic energy

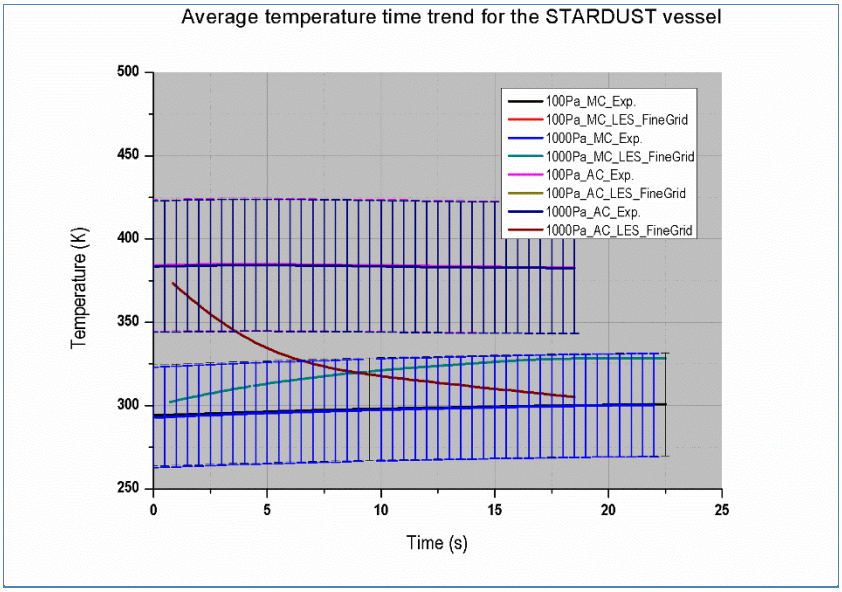

Fig.8 Numeric average temperature time trend for the STARDUST vessel

For the MC cases the average temperature increases from ambient temperature (294 K) to 328 K (11%) in about 22 s. For the AC cases the average temperature decreases from initial internal temperature (384 K) to 305 K (12%) in about 18 s. Results appear to be concordant, as simulations satisfactorily reproduce experimental results only for MC case. Agreement seems to be poor for AC case. Fig.15 shows the calculated temperature field inside the domain. This poor agreement may be caused by thermal high thermal inertia of TJ thermocouple. The effect of wall temperature and initial internal pressure on pressurization rate and filling time is summarized in Table 12.

Effect of wall temperature and initial internal pressure on pressurization rate			
Effect	**Experimental**	**Analytic**	**Numeric**
Internal pressure	4,69%	Insensible	4,74%
Wall temperature	16,12%	23,62%	16,49%
Effect of wall temperature and initial internal pressure on filling time			
Effect	**Experimental**	**Analytic**	**Numeric**
Internal pressure	-2,22%	-1,08%	1,81%
Wall temperature	-17,78%	-12,94%	-19,11%

Table 12: Effect of wall temperature and initial internal pressure on pressurization rate and filling time

Global results comparison gives a significant indication. In the LOVA CFD simulation, wall and internal temperatures play a more important role than the initial internal pressure variation.

4. Numerical analysis for multiphase flow

4.1. Numerical problem setting

The contemporary presence of different phases is common in many industrial applications. The multiphase [32] flows (i.e. systems in which different fluid and solid phases are simultaneously present) are common during the normal operation and when an accident occurs. These kind of flows could be involved inside large vacuum vessel during a LOVA event, so methods for predicting their behavior is a key factor in nuclear reactor safety. Rapid mobilization of large

quantities of dust in this scenario would provide a large surface area for chemical reactions (i.e. dust explosion) and may also result in the release of dust through the breach. Thus, understanding aerosol mobilization in a LOVA is prerequisite to assessing the safety hazards. During this accidental transient, the air ingress generates complex dust mobilization and transport phenomena in the vessel. In this study, our concerns are focused on preliminary modeling of the first instant of dust mobilization during a LOVA event. We tried to simulate the amount of particle only as a crude prediction of the dispersion of particle. This numerical approach is very effective to estimate quantitatively the dust mobilization during the LOVA when the large scale experiments are not easy to perform. A simulation of LOVA event in STARDUST with W dusts mobilization by means of the ANSYS-CFX code is performed. The focus of these re-suspension analyses is the predictions of the dust volume fraction inside vessel for the first instant of LOVA and the mobilization fraction on the tray were the dust are placed. In present work multiphase flow [33] is treated using the Eulerian-Eulerian two-fluid model [34]: the flow is considered to be turbulent with no interphase mass transfer. The LOVA accident scenarios in large vacuum systems could involve large quantities (kilograms) of dust [43]. This precludes a treatment of individual particles, so we treat the particles as a continuum fluid. The Eulerian technique, applied to dispersed phase generally treats the particles in the same manner of the continuum phase, using the same discretization too. The inhomogeneous model is used (i.e. each fluid possesses its own flow field and the fluids interact via interphase transfer terms). Interfacial transfer of momentum, heat and mass is directly dependent on the contact area between the two phases. This is characterized by the interfacial area per unit volume between phase α and phase β (i.e. interfacial area density, $A_{\alpha\beta}$). Particle model is used for the interfacial transfer. This model essentially provides the algebraic prescriptions for the interfacial area density. The particle model assumes that one of the phases is continuous (phase α) and the other is dispersed (phase β). The surface area per unit volume (7) is then calculated by assuming that phase β is present as spherical particles of mean diameter equal to d_β. Using this model a simplified expression for the interfacial area density can be written as:

$$A_{\alpha\beta} = \frac{6\phi_\beta}{d_\beta} \tag{7}$$

where ϕ_β is the volume fraction of the dispersed phase. Non-dimensional interphase transfer coefficients may be correlated in terms of the particle Reynolds number (8) and the fluid Prandtl number (9). These are defined using the particle average diameter and the continuous phase

properties, as follows:

$$\mathrm{Re}_{\alpha\beta} = \frac{\rho_\alpha |u_\beta - u_\alpha| d_\beta}{\mu_\alpha} \tag{8}$$

$$\mathrm{Pr}_{\alpha\beta} = \frac{u_\alpha C_{p\alpha}}{\lambda_\alpha} \tag{9}$$

The k-ε model turbulence model is used for the continuous phase. The dispersed phase zero equation is used for the dispersed phase. The eddy viscosity hypothesis is assumed for each turbulent phase. Diffusion of momentum in continuous phase is governed by an effective viscosity. The default zero-equation model uses a formula based on geometric length scale and the average solution velocity. It is correlated for single-phase turbulent pipe flow. The turbulence viscosity (10) is modeled as the product of a turbulent velocity scale $U_{t\alpha}$, and a turbulence length scale $l_{t\alpha}$, as proposed by Prandtl and Kolmogorov:

$$\mu_{t\alpha} = \rho_\alpha f_\mu U_\alpha l_{t\alpha} \tag{10}$$

where f_μ is a proportionality constant. The velocity scale is calculated to be the maximum velocity in continuous phase. The length scale (11) is derived using the formula:

$$l_{t\alpha} = \frac{V_D^{1/3}}{7} \tag{11}$$

where V_D is the fluid domain volume. In the Dispersed Phase Zero Equation Model the parameter turbulent Prandtl σ number correlates the dispersed phase kinematic eddy viscosity ν_{td} (12) to the continuous phase kinematic eddy viscosity ν_{tc}:

$$\nu_{td} = \frac{\nu_{tc}}{\sigma} \Longrightarrow \mu_{td} = \frac{\rho_d}{\rho_c}\frac{\nu_{tc}}{\sigma} \tag{12}$$

The drag exerted on an immersed body by a moving fluid arises from two mechanisms only. The first is due to the viscous surface shear stress, namely skin friction. The second is due to the pressure distribution around the body, namely form drag. The total drag force can be expressed in terms of the adimensional drag coefficient C_D. For a particle of simple shape, immersed in a Newtonian fluid and which is not rotating relative to the surrounding free stream, the drag

coefficient C_D depends only on the particle Reynolds number. The function $C_D(Re_\alpha)$ may be determined experimentally, and it is known as the drag curve. A commonly used drag model for densely distributed solid particles is the Wen Yu Drag Model [35]. The Wen Yu correlation is valid for solid volume fractions bigger than 0.2. The drag coefficient (13) is defined as:

$$C_D = \phi_c^{-1.65} \max\left(\frac{24}{\phi_c Re}(1 + 0.15(\phi Re)^{0.687}, 0.44)\right) \tag{13}$$

ϕ_c is the continuous phase volume fraction. For very dense gas-solid or liquid-solid flows, such as those that occur in fluidized bed applications, the Gidaspow correlation (13b) can be used. This correlation uses the Wen Yu correlation for low solid volume fractions $\phi_d < 0.2$, and switches to Ergun's law for larger solid fractions.

$$c_{\alpha\beta}^{(d)} = 150\frac{(1-\phi_c)^2\mu_c}{\phi_c d_p^2} + \frac{7}{4}\frac{(1-\phi_c)\rho_c|U_c - U_d|}{d_p} \tag{13b}$$

The Gidaspow drag model is used in this setup. The drag force F_D (14) is expressed as a function of drag coefficient C_D, projected area of particle A, continuum phase velocity v_f and dust particle velocity v_f:

$$F_D = \frac{1}{2}\rho_f A C_D |v_f - v_p|(v_f - v_p) \tag{14}$$

The CFD model used in this work is based on the extended two fluid models, the Gidaspow solids pressure model to describe particle-particle interactions is simulated. In the solids pressure model the forces due to solid collisions are taken into account by introducing additional solids pressure and solids stress terms into the solid phase momentum equation based on the Gidaspow model. The collisional solids stress tensor in the solid phase momentum equation (15) is defined as:

$$\tau_{sij} = -P_s\delta_{ij} + \mu_s\left(\frac{\partial U_i}{\partial x_j} + \frac{\partial U_j}{\partial x_i} - \frac{2}{3}\frac{\partial U_k}{\partial x_k}\delta_{ij}\right) + \zeta_s\frac{\partial U_k}{\partial x_k}\delta_{ij} \tag{15}$$

Where P_s denotes solids pressure, μ_s denotes solids shear viscosity and $\zeta_s$denotes solids bulk viscosity. The most common equations for solids pressure are due to Gidaspow. These specify the solids pressure gradient rather than solids pressure directly (15):

$$P_s = P_s(\phi_s) \Longrightarrow \nabla P_s = G(\phi_s)\nabla\phi_s = G_0 e^{c(\phi_s - \phi_{s,max})}\nabla\phi_s \quad (15)$$

where $G(\phi_s)$ is the elasticity modulus, G_0 is the reference elasticity modulus, c is the compaction modulus, and $\phi_{s,max}$is the maximum packing parameter. The maximum packing parameter is the volume fraction of the solid phase at its state of maximum packing. For a dispersed solid phase the maximum packing fraction may range from 0.5 to 0.74, the latter being the maximum possible packing for solid spheres.

A simulation W dusts mobilization inside STARDUST facility by means of the ANSYS-CFX code is performed using the domain discretization illustrated for the LOVA model validation. The objective of these re-suspension analyses is to predict the W dusts volume fraction inside vessel for the first instant of LOVA and the mobilized fraction of the sample placed on the tray (Fig.16).

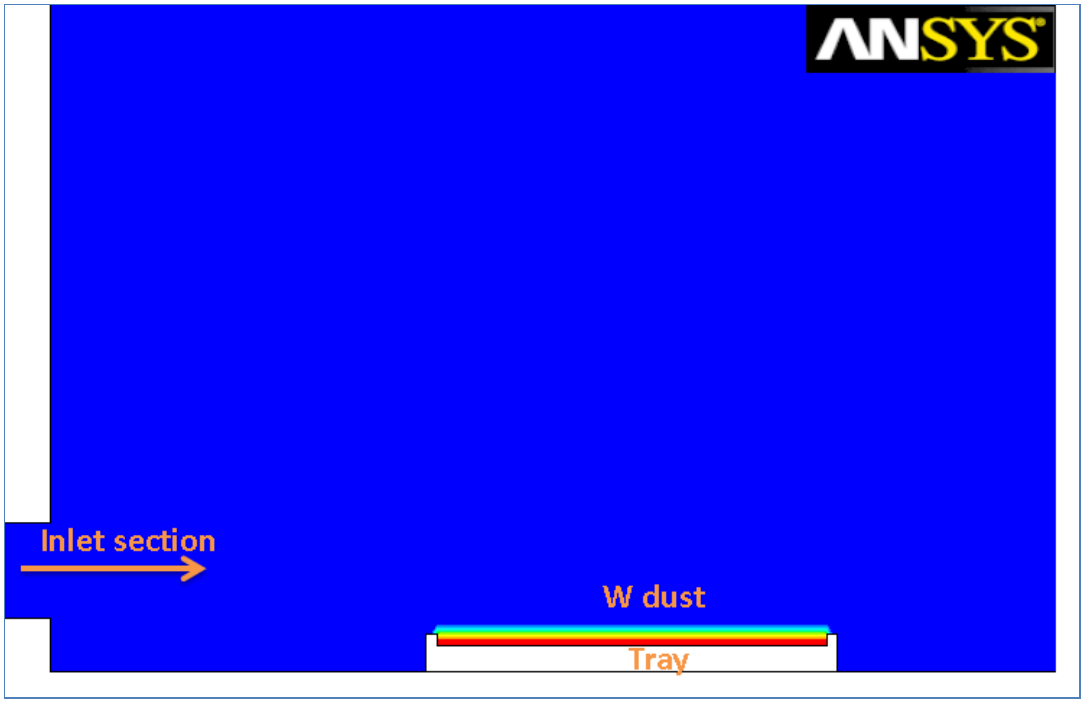

Fig.16 W dust on the tray inside the computational domain (2D section)

Major assumptions on the dust mobilization phenomenon are as follows:

- Dust particles are spherical in shape
- All dust particles have the same size and same specific heat
- Motion of the dust particles is governed by their inertia and drag forces in the fluid

- Phase transformation does not occur
- Dust particles are isothermal having no temperature gradients in the radial direction
- No surface forces such as van der Waals force, particle wetness and electrostatic charges are considered

The internal components of the vessel were not simulated in present STARDUST experimental campaign and simulation. This simplification can eliminate the effect of the internal components on the dust mobilization and then it is more conservative. The present numerical study is performed under the condition that the breach is just at the bottom of the vessel (valve B). This configuration is a more conservative assumption causing a higher dust mobilization. The input conditions for the fluid are as follows: initial pressure in the vessel 100Pa; wall temperature in the vessel 296K. External fluid outside the vessel is air of P=101325 Pa and T=296K. The flow rate inlet function is imposed at the inlet boundary in order to obtain the constant pressurization rate of 300 Pa/s. In present simulation no-slip and boundary conditions are adopted to the walls in the whole domain.

The granulometry of the W particles is constant and around the average values provided by the SEM (0.4μm). Dusts are placed inside the domain on the tray (25 cm^2) on the floor of vessel at about 5cm from the inlet section with null initial velocity. The input conditions were set up based on an assumption that the fluid is in the continuum. The operating fluid used in the simulations was dry air assumed initially at rest. The density of the fluid was evaluated using the standard Redlich Kwong real gas and the other thermodynamic properties were considered variable according to internal database.

4.2 Numerical results

For the LOVA simulation, consistently with the air flux at the inlet of the domain (set as mentioned), the obtained difference of average pressure ΔP (t) inside the vessel shows, as required, a linear trend with expected slope for all simulation [43, 44].

The axial velocity evaluated close to the air injection increases from zero to the maximum in the first second and then decreases [43, 44]. The CFD applications show stable numerical results for modeling local gas velocity field at low pressure conditions. The calculated data show a satisfying global agreement with experimental data for all performed experiments and simulations [43, 44]. Velocities remain very high for all transients (see axial velocity values at Fig.17).

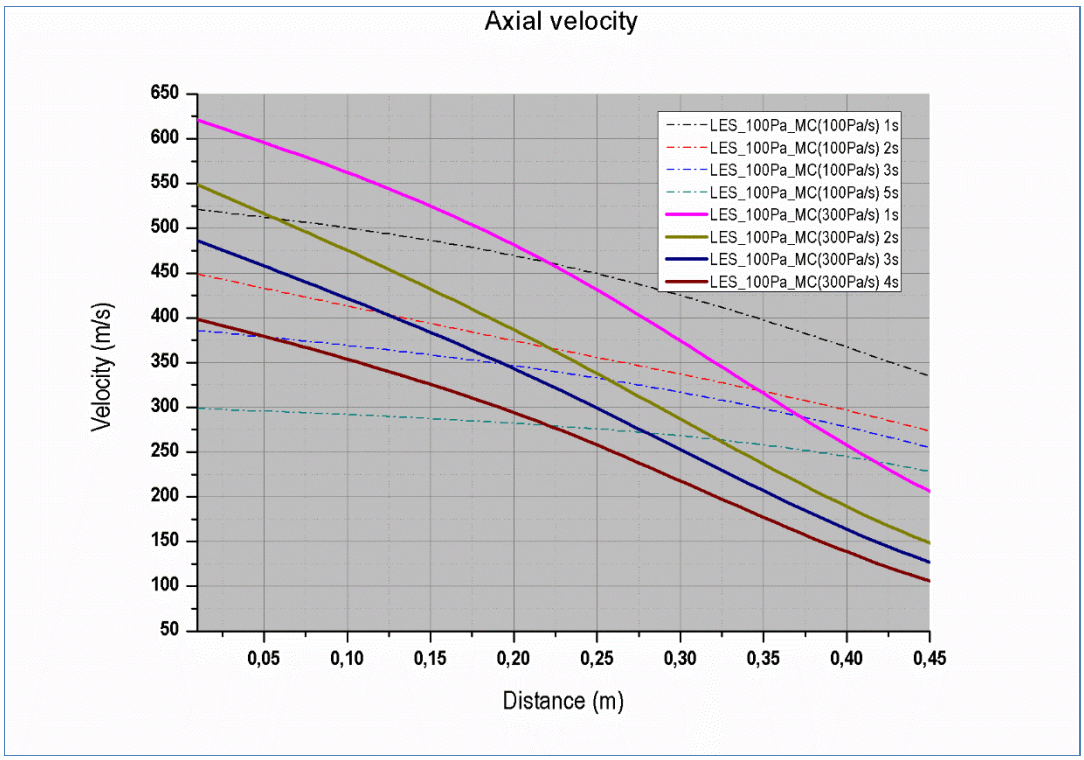

Fig.17 Axial velocity along injection axis for 100Pa/s and 300 Pa/s case

The calculated data show a satisfying global agreement with experimental data for all the performed experiments and simulation (from 1/3 to 2/3 of the vessel length the differences are about 33%) [see the velocity profiles on line 1 and line 3 in Fig.18 and on line 4 and line 7 in Fig.19].

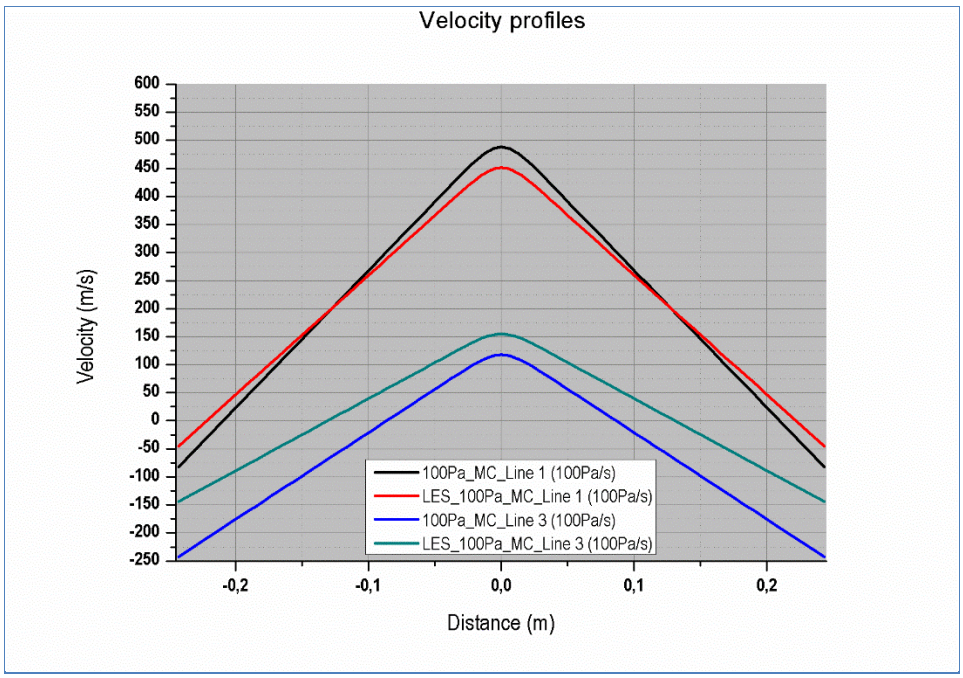

Fig.18 Velocity profiles for Line 1 and Line 3 at 1s(100Pa, 100Pa/s, Mc)

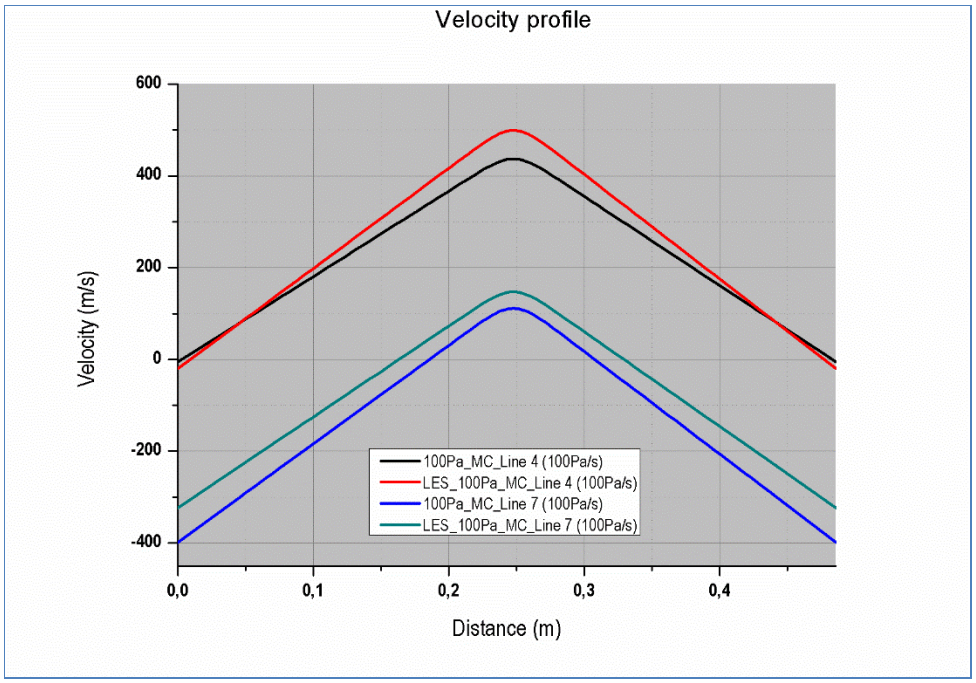

Fig.19 Velocity profiles for Line 4 and Line 7 at 1s (100Pa, 100Pa/s, Mc)

The high axial velocity region close to the air inlet corresponds to the expansion jet flow area. A recirculating flow can be observed close to the right side of the cylindrical wall (negative axial velocity). The code is able to assess the radial velocity that can't be detected during the

experimental tests. The numerical results for the radial velocity predicted E, F and G (for points along the injection axis is practically zero) are reported in Fig.20.

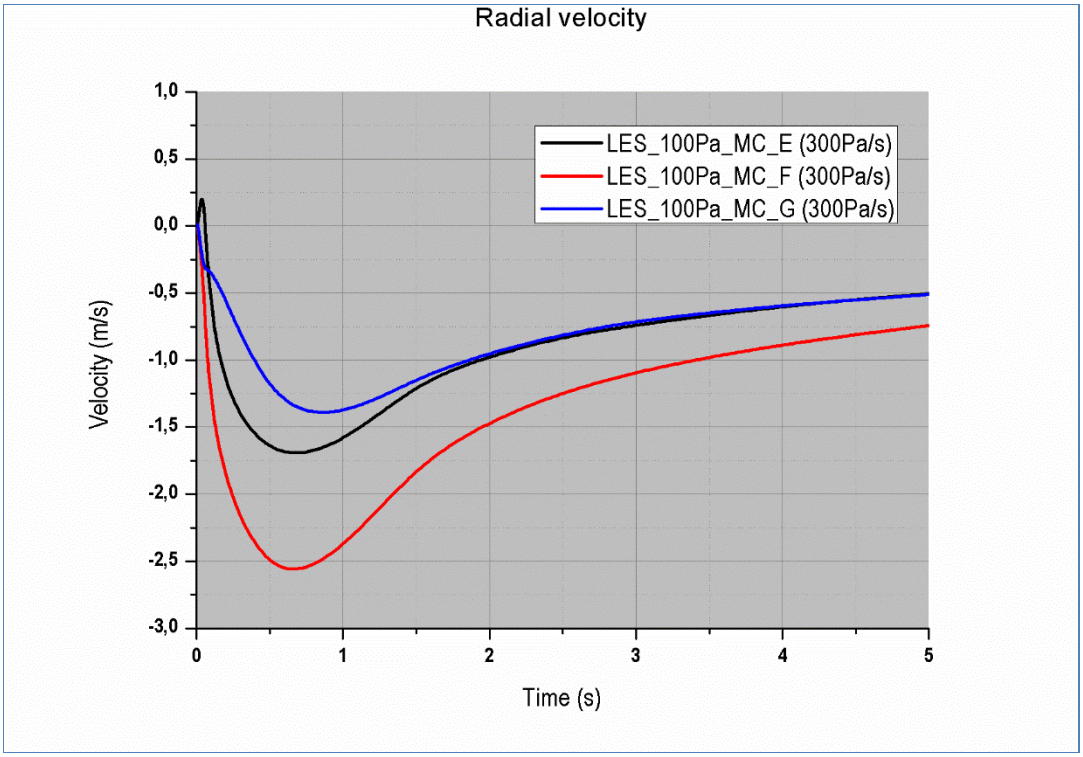

Fig.20 Radial velocity

Observing the velocity profile inside the vessel we can see a reduction of axial velocity at point for 500Pa/s pressurization rate case (Fig.21 shows the reduction for point A, but it is similar for all points) [44]. This is caused by the typical compressible flow effect named choked effect. In the case of high upstream air pressure and vacuum conditions downstream of an inlet section (orifice), both the air velocity and the mass flow rate become limited when sonic velocity is reached through the inlet section and the expansion inside the vessel becomes limited [40].This effect can be appreciate in Fig.22 where the maximum numerical velocity is plotted versus the pressurization rate imposed.

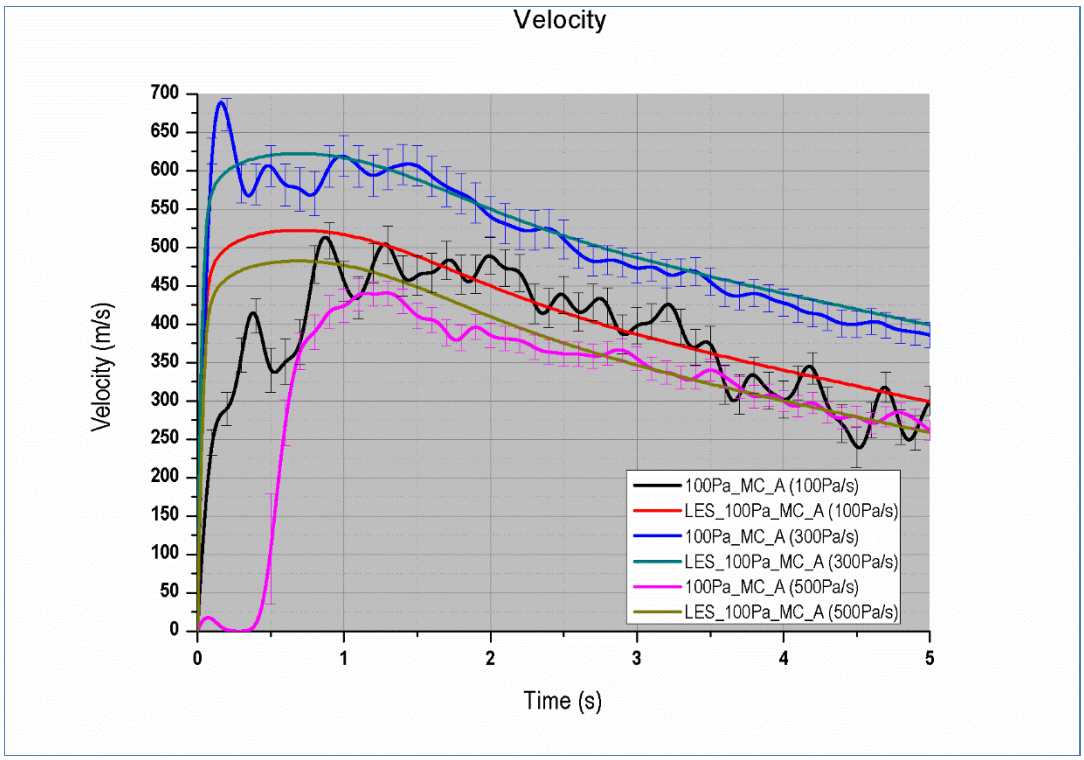

Fig.21 Velocity history for different pressurization rates for point A

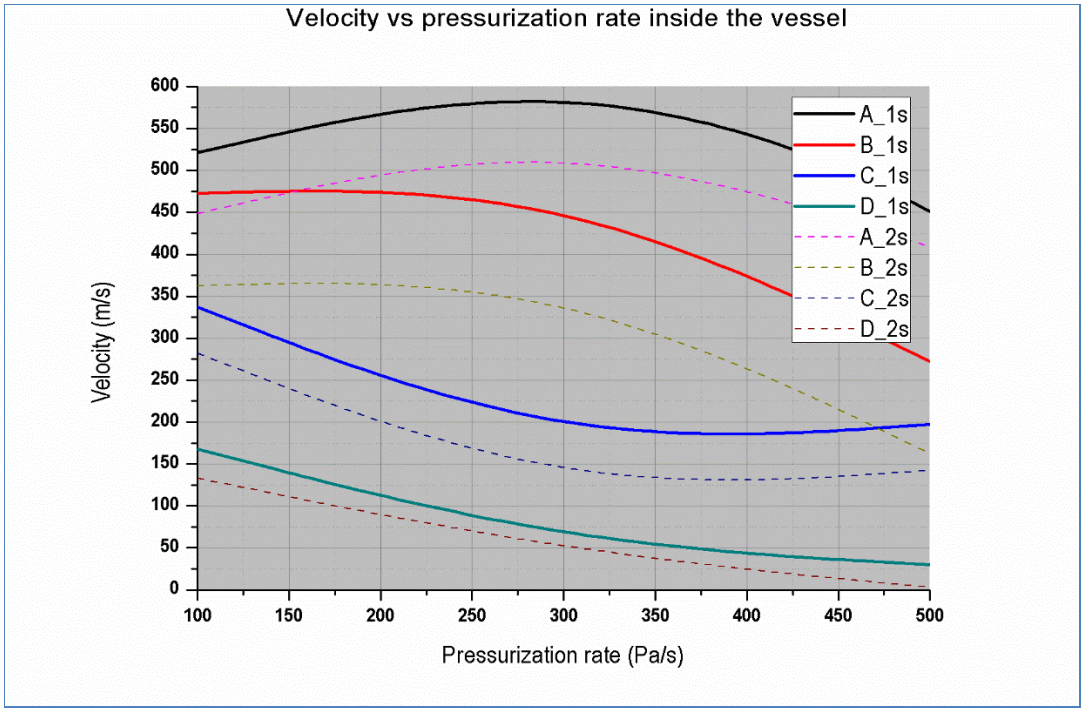

Fig.22 Velocity vs pressurization rate inside the vessel for point A B C and D

This means that the highest velocities, that are the driver parameter for dust mobilization inside

the vessel, are reached for low pressurization rate around 300 Pa/s (Fig.23).

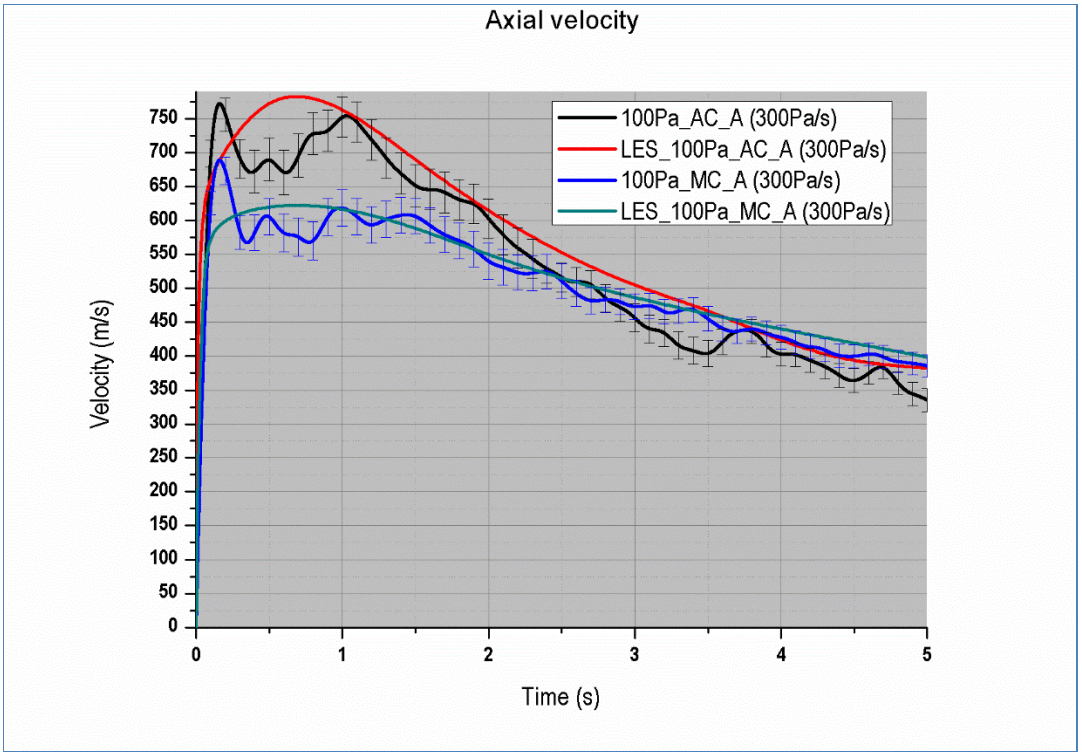

Fig.23 Axial velocity for MC and AC case (Point A)

The calculations show that the air velocities always increase when the vessel is heated (AC). The air velocity reaches its peak value, 770 m/s for 300 Pa/s AC case, at about 0.7 s. This is a negative result from the safety view point because an accident during the normal operation can mobilize a higher amount of dust. If the temperature of the air becomes higher, air density becomes lower, which would create a higher air velocity in the vessel. However, with the increase of the temperature the viscosity of the gas increases and the pressure loss is proportional to the velocity squared. In other words, the resistance increases much slower than the density reduction with the increase of the average temperature. The net effect is a reduction in air ingress velocity as temperature rises.

It is possible to compare the temperatures obtained by LES with the temperatures measured inside the STARDUST vessel. No increase is detected by the thermocouples in experiments during the whole pressurization transient. In order to explain better the average temperature time trend shown in Fig.24, we assumed valid the adiabatic unsteady analytical model again. Fig.24 shows the average temperature trend obtained from adiabatic unsteady model compared to the data calculated with ANSYS-CFX code.

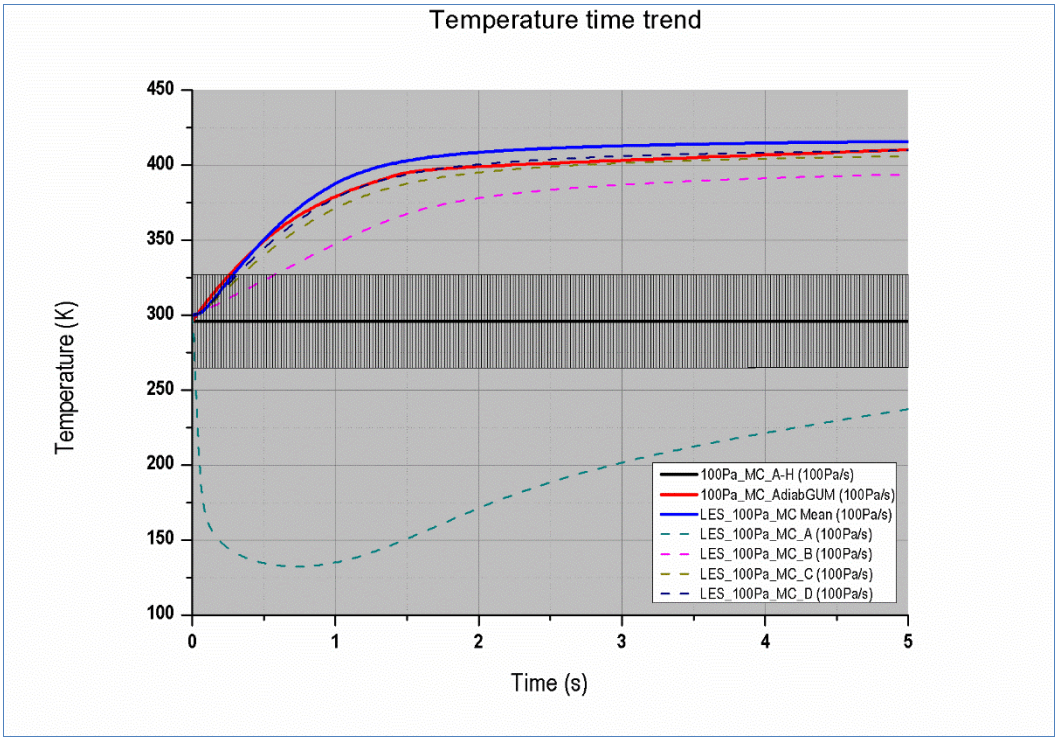

Fig.24 Temperature time trend

Analytical data well agree with CFD results and both the trends show how temperature increases because the flow work (associated with the pressure at the inlet section) is converted in internal energy (final temperature is $T_{final} \approx \gamma T_{initial}$). The results for the local values of temperature for the six monitor points are also showed in Fig.28 and Fig.25. Data calculated using LES for point A, placed very close to the inlet section and then near the expansion zone showing a sharp drop in the first second of simulation with a minimum of about 130 K after that temperature increases.

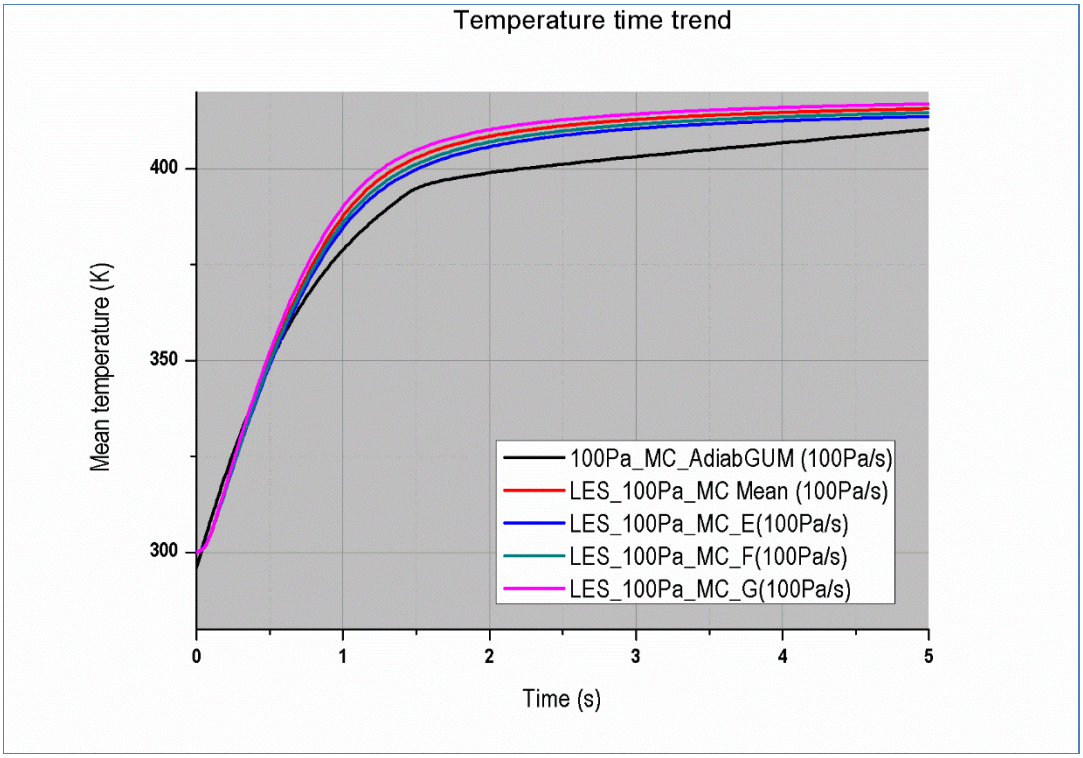

Fig.25 Local values of temperature

The other point shows different temperature behavior compared to the other monitor points, because they are located far enough from the inlet section. In fact, these monitor points are characterized by a temperature increase from the beginning of the simulation. From the analysis of temperature time trends reported we can conclude that local temperature variations near the inlet section are very strong and a detailed experimental analysis is necessary in order to confirm this behavior. The preliminary investigation about of dust transport and mobilization of the 0.4 μm W dust in condition of medium pressurization (300 Pa/s) is performed. Fig.26 shows the predicted simulation fraction.

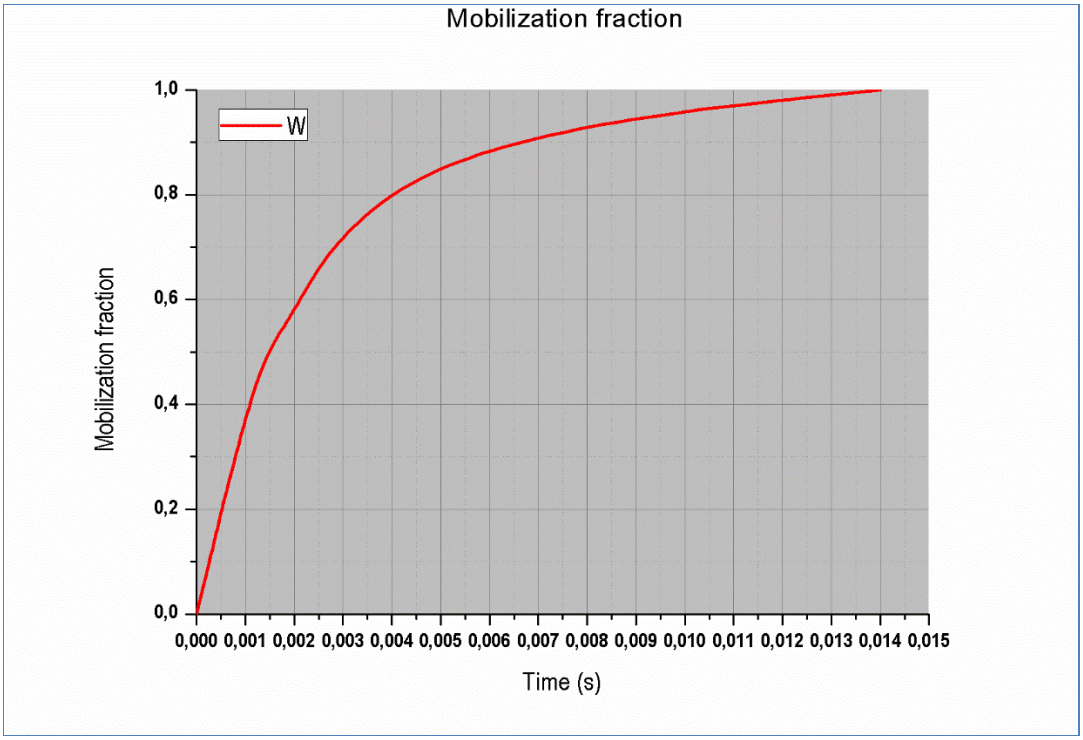

Fig.26 Predicted mobilization fraction as a function of time for 0.4μm W dust and pressurization rate 300 Pa/s

Fig.27 and Fig.28 present a 2D planar section of STARDUST domain showing the air and dust velocity obtained for the 0.4μm W dust dispersion after 0.0018 s from the air injection.

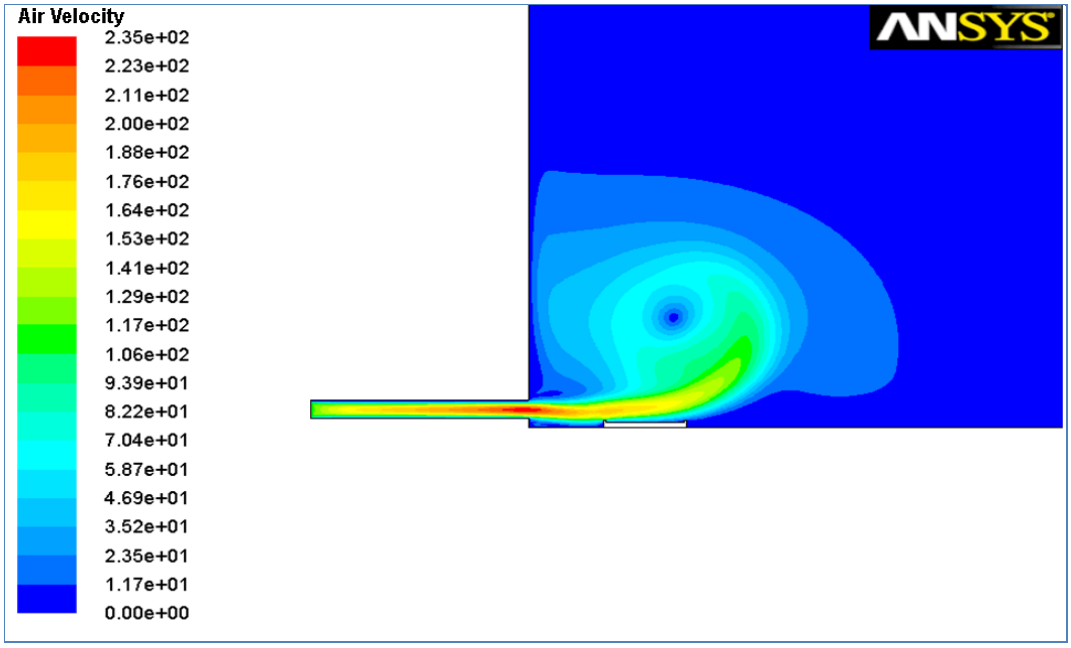

Fig.27 Air velocity obtained for the 0.4μm W dust dispersion after 0.0018s from the air injection

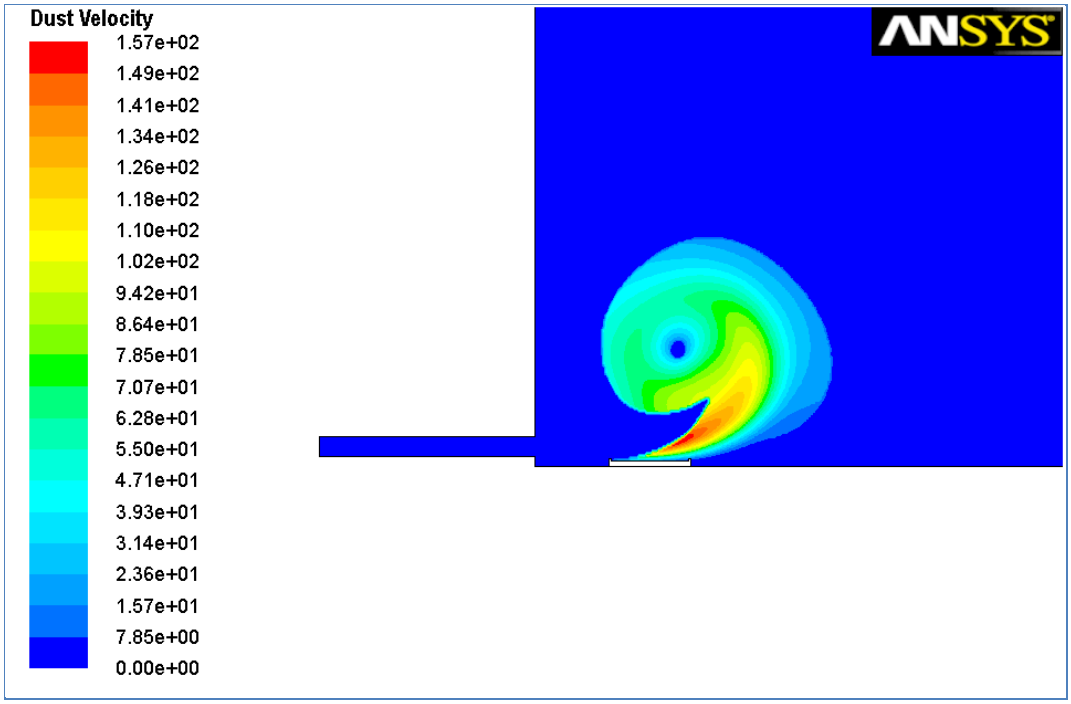

Fig.28 Dust velocity obtained for the 0.4μm W dust dispersion after 0.0018s from the air injection

Fig.29 and Fig.30 show the calculations results of dust volume fraction evolution. After the impact dusts from tray approach the vortices generated by jet and are lifted up and quickly reach the upper wall.

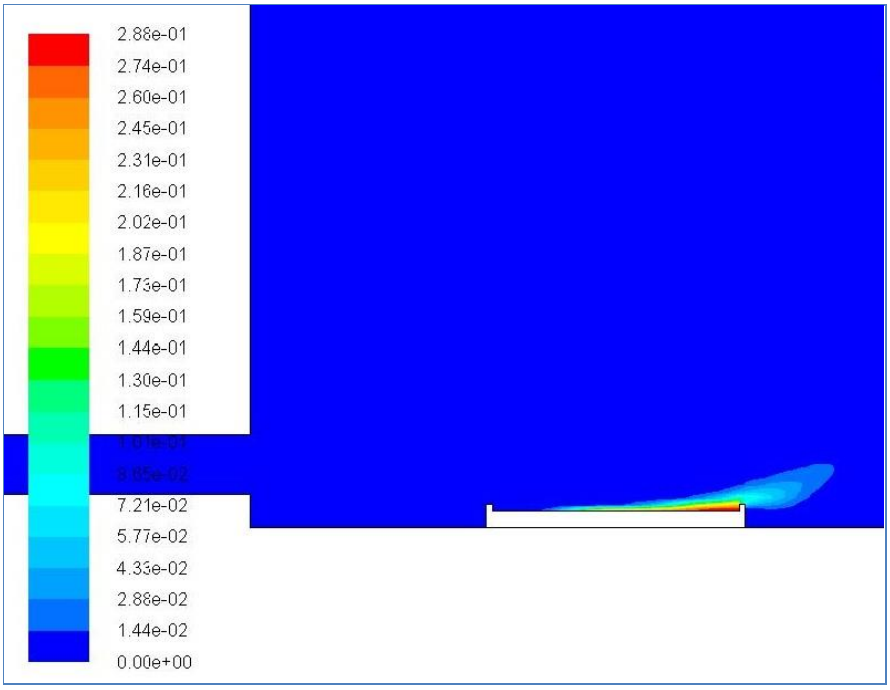

Fig.29 Dust volume fraction obtained for the 0.4μm W dust dispersion after 0.0018s from the air injection

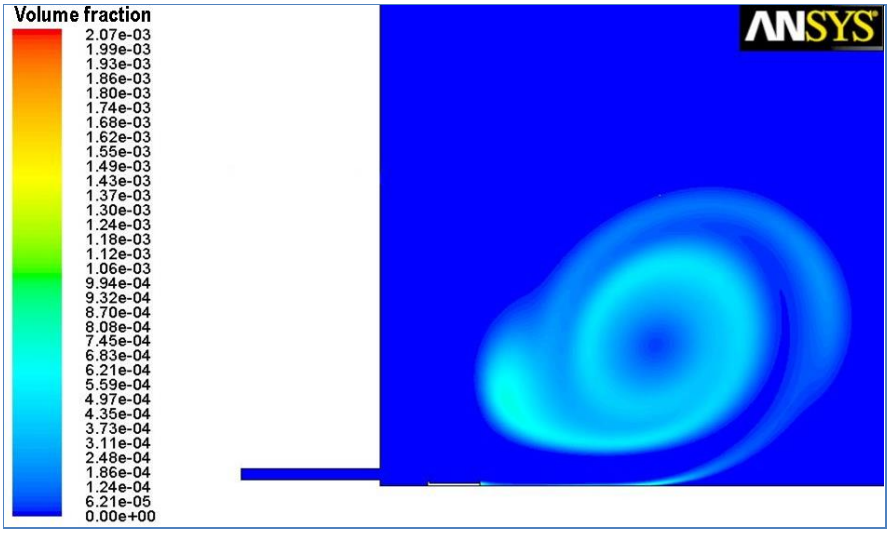

Fig.30 Volume fraction of 0.4μm W dust after 0.014s from air injection

Conclusions

The aim of this work was to contribute towards improving the understanding of processes taking place during a LOVA event. A CFD model was developed and validated. This model simulates the complex thermo fluid-dynamic field and provides some indication about dust mobilization during a vessel filling at near vacuum conditions for supporting understanding of phenomena occurring during the first instants of a LOVA event in large vacuum systems. The CFD simulation and experimental activities have been carried out in strong correlation in order to understand the capabilities of computational codes and also to correctly predict flow characteristics during a LOVA event. The limits of a commercial code ANSYS-CFX for modeling the first instants of LOVA event have been evidenced. The LES computations show a better agreement with the experiments than RANS for modeling local gas velocity field at low pressure conditions. However, computations become less accurate studying the average temperature time trend inside the vessel. This lack of precision between experimental data and CFD results must be ascribed to the difficulty in measuring such parameters with reasonable precision for these particular flow conditions. An improvement in the detail and precision of the experimental analysis will be necessary in order to fix this problem. The models have shown

very promising results, especially in terms of accuracy and quality of analysis. A preliminary investigation of dust transport and mobilization of the 0.4μm W dust in condition of medium pressurization (300 Pa/s) has been performed. A new geometry configuration of STARDUST has been proposed.

Conflict of interest

The authors declare that they have no conflict of interest.

Acknowledgements

We want to acknowledge Quantum Electronics Plasma Physics and Materials (QEPM) Research Group (Department of Industrial Engineering, University of Rome Tor Vergata) and the researchers involved in safety and security at ENEA FUS TECH (Frascati, Rome).

References

1. R. Toschi, Fusion Eng. Des. 36, 1–8 (1997)
2. A.V. Chankin et al., J. Nucl. Mater. 290-293 (2001)
3. S.K. Erents, Fusion 42, 905 (2000)
4. N. Asakura, Phys. Rev. Lett. 84, 3093 (2000)
5. S.J. Piet, G. Federici, ITER Rep. S 81 RI 13 96-06-28 W 1.4. (1996)
6. J.P. Sharpe, D.A. Petti, H.-W. Bartels, Fusion Eng. Des., 63–64, 153–163 (2002)
7. J.Winter, Phys. Plasmas, 7, 3862–3866 (2000)
8. T. Honda et al., Fusion Eng. Des. 47, 361-375 (2000)
9. E. Eberta, J. Raeder, Fusion Eng. Des. 17, 307-312 (1991)
10. K. Matsuki et al., Fusion Eng. Des. 81, 1347–1351 (2006)
11. J.P. Van Dorsselaere et al. Fusion Eng. Des. 84, 1905–1911 (2009)
12. P. Gaudio, A. Malizia, I. Lupelli, (2010), In Proc. Int. Conf. on Math. Models for Eng. Science, 134-147 (2010)
13. M. Benedetti et al., Fusion Eng. Des. 88, 2665-2668 (2013)
14. C. Bellecci et al., Fusion Eng. Des. 86, 2774-2778 (2011)
15. C. Bellecci et al., Nucl. Fusion, 51, 053017 (2011)
16. C. Bellecci et al., Fusion Eng. Des. 86, 330-340 (2011)

17. M. Benedetti et al., In Proc. 2nd Int. Conf. on FLUIDSHEAT'11 TAM'11. In Proc. 4th WSEAS Int. Conf. UPT'11 CUHT'11, 142-147 (2011)
18. C. Bellecci et al., In Proc. 37th EPS Conf. on Plasma Physics 34, 703-706 (2010)
19. P. Gaudio, A. Malizia, I. Lupelli, In Proc. Int. Conf. on Math. Models for Eng. Science (MMES'10), 134-147 (2010)
20. C. Bellecci et al., 36th EPS Conf. on Plasma Physics 33, 266-269 (2009)
21. C. Bellecci et al., 35th EPS Conf. on Plasma Physics 32, P-1.175 (2008)
22. ITER Joint Central Team, General Safety and Security Report (GSSR) G 84 RI 1 01-07-09 R 1.0. (IAEA, 2001), https://fusion.gat.com/iter/iter-fdr/final-report-sep-2001/Plant_Assembly_Documents_%28PADs%29/Generic_Site_Safety_Report_GSSR/GSSR_09_ExtHazAssmnt.pdf Accessed 6 February 2015.
23. T. Pinna et al., Fusion Eng. Des. 85, 1410-1415 (2010)
24. M. Benedetti et al., Fusion Eng. Des. 88, 2665-2668 (2013)
25. ANSYS CFX-Solver Theory Guide (ANSYS, Inc., Canonsburg, PA, USA, 2009)
26. A.K. Majumdar, Generalized Unsteady Solution of Isentropic and Isothermal Pressurization Process (NASA-CR 204244, Huntsville, Alabama, USA, 1990)
27. G. Van Wylen, L. Sonntag, Fundamentals of Classical Thermodynamics (John Wiley & Sons, 1976)
28. Peter V. Nielsen, F. Allard, H. B. Awbi, L. Davidson, A. Schälin, Fluidodinamica Computazionale (Dario Flaccoro Editore, Italy, 2009)
29. A. Quarteroni, Modellistica numerica per problemi differenziali (Springer Italia, 2008)
30. F. Thompson, B.K. Soni, N.P. Weatherill, Handbook of Grid Generation (CRC Press LLC, 1999)
31. H. S. Mukunda, Direct simulation of high-speed mixing layers (NASA Technical Paper 3186, 1992)
32. P. Incropera, Fundamentals of Heat and Mass Transfer, 7th edn. (Wiley, 2012)
33. D. Chiappini, Numerical Analysis of Multiphase Flows through the Lattice Boltzmann Method (PhD Thesis, Department of Industrial Engineering, University of Rome Tor Vergata, 2010)
34. E.D. Fatnes, Numerical simulations of the flow and plugging behaviour of hydrate particles (Department of Physics and Technology, University of Bergen, 2010)
35. D. Pfleger, Chem. Eng. 54, 5091-5099 (1999)
36. C.J. Chen, S.Y. Jaw, Fundamental of turbulence modeling (CRC Press, 1997)

37. D.C. Wilcox, Turbulence Modeling for CFD, (DCW Industries, La Canada, CA, USA, 1994)
38. R.A. Andersson, Fluid Dynamics for Engineers (Cambridge, 2012)
39. S. Crist, P.M. Sherman, Study of highly underexpanded sonic jet (AIAA Journal, 1966)
40. C.D. Wilcox, Multiscale model for turbulent flows (AIAA 24th Aerospace Sciences Meeting, American Institute of Aeronautics and Astronautics, 1986)
41. A. Malizia et al., Fusion Eng. Des. (2014) doi: http://10.1016/j.fusengdes.2014.01.014
42. P. Gaudio et al., In Proc. Int. Conf. Frontiers in Diagnostic Tech., INFN-Frascati, Rome (2013)
43. A. Malizia et al., Adv. Mater. Sci. Eng. (2014) http://dx.doi.org/10.1155/2014/201831
44. I. Lupelli et al., Fusion Eng. Des. (2014) doi: 10.1016/j.fusengdes.2014.03.064